ANALYSIS OF NUMERICALLY INDUCED OSCILLATIONS IN 2D FINITE-ELEMENT SHALLOW-WATER MODELS PART I: INERTIA-GRAVITY WAVES[*]

DANIEL Y. LE ROUX[†], VIRGILE ROSTAND[†], AND BENOIT POULIOT[†]

Abstract. The numerical approximation of shallow-water models is a delicate problem. For most of the discretization schemes, the coupling between the momentum and the continuity equations usually leads to anomalous dispersion in the representation of fast waves. A dispersion relation analysis is employed here to ascertain the presence and determine the form of spurious modes as well as the dispersive nature of the finite-element Galerkin mixed formulation of the two-dimensional linearized shallow-water equations. Nine popular finite-element pairs are considered using a variety of mixed interpolation schemes. For each pair the frequency or dispersion relation is obtained and analyzed, and the dispersion properties are compared analytically and graphically with the continuous case. It is shown that certain choices of mixed interpolation schemes may lead to significant phase and group velocity errors and spurious solutions in the calculation of fast waves. The $P_1^{NC} - P_1$ and RT0 pairs are identified as a promising compromise, provided the grid resolution is high relative to the Rossby radius of deformation for the RT0 element. The numerical solutions of two test problems to simulate fast waves are in good agreement with the analytical results.

Key words. shallow-water equations, finite-element method, dispersion analysis, surface waves

AMS subject classifications. 35L99, 74S05, 65T99, 74J15

DOI. 10.1137/060650106

1. Introduction. The shallow-water (SW) equations describe the behavior of a shallow homogeneous incompressible and inviscid fluid layer. They are derived from the depth-averaged Navier–Stokes equations under Boussinesq and hydrostatic pressure assumptions. The SW system is extensively used in environmental studies to model hydrodynamics in lakes, estuaries, coastal regions, and other applications.

Galerkin techniques have gradually evolved to become a popular method for this problem class including the finite-element (FE) [14, 18, 27, 31, 32, 36, 44], the spectral-element [28, 43], the finite-volume (FV) [4, 15, 16, 19, 26], and the discontinuous Galerkin [3, 8, 17, 20, 41] methods. Indeed, unstructured elements offer the enhanced flexibility of using grids of variable sizes, shapes, and orientation for representing the boundaries of complex domains and a natural treatment of boundary conditions. Calculations on graded meshes of unstructured grids are hence standard practice [5, 18, 19, 20, 33, 46, 47].

For most numerical methods, including the finite-difference (FD), FV, and FE schemes, the coupling between the momentum and continuity equations is a delicate problem. One of the issues associated with mixed formulations is the possibility of spurious modes that may arise for certain choices of grids and bases. For example, the piecewise linear Galerkin discretization of the SW equations (for velocity and elevation variables) is usually plagued by spurious oscillations [28, 45]. The appearance of such oscillations is mainly due to an inappropriate placement of variables on the grid and/or a bad choice of approximation function spaces. Improvements have been achieved

[†]Département de Mathématiques et de Statistique, Université Laval, Québec G1K 7P4, QC, Canada (dleroux@mat.ulaval.ca, vrostand@mat.ulaval.ca, bpouliot@giref.ulaval.ca).

through the use of suitable FD grids [6, 39], a variety of mixed-order FE interpolation schemes [2, 28, 27, 32, 33, 48], and a wave equation formulation [29, 36].

This difficulty with mixed methods is not specific to the SW problem alone but is well known also in other contexts such as primitive variable viscous flows where it has been extensively investigated for the Galerkin FE method [13, 23]. However, the situation in the mixed SW problem is different and, as noted initially in [45] and in subsequent studies [27, 32, 47], an analysis of the dispersion relation for a given formulation will explicitly ascertain the presence and determine the form of spurious modes as well as the dissipative/dispersive nature of a given formulation.

The dispersion relation analysis assumes that the solution of the differential equations can be separated and formulated as periodic in space and time. It differs from the Fourier analysis in that the time variable remains continuous by using the harmonic form of the equations. Consequently, a Fourier expansion is performed only for the nodal unknowns that appear in the discrete equations. The analysis results in a dispersion relation where the magnitude of the temporal frequency is expressed in terms of wave numbers. Such a technique was applied early on to the SW model in [38].

Two-dimensional dispersion analysis of FE SW discretizations using the same linear basis functions for all variables was examined first. One grid configuration is considered in [45], while the influence of grid configuration on the dispersion properties is analyzed in [9, 10, 21] for the mixed primitive variable form and in [37] in the case of the wave equation formulation. Phase behavior of FV SW discretizations has been studied in [24, 42]. To our knowledge, the two-dimensional dispersion relation analysis of the SW equations using the $P_1^{NC} - P_1$ FE pair [35] was the first study analyzing the dispersion relation of a FE scheme using different approximation spaces for the velocity and surface-elevation fields on meshes made up of triangles. The aim of the present study is to extend the two-dimensional dispersion relation analysis of the FE SW equations to a variety of mixed-order interpolation schemes. Because all the aforementioned problems occur primarily in the context of linear formulations, solving linear equations is sufficient for our purpose.

The paper is developed as follows: The linear SW equations and the Galerkin FE discretization schemes are presented in section 2. The discrete operators are computed in section 3 and the dispersion relations are obtained. The latter are compared analytically and graphically with the continuous case in section 4. This dispersion analysis is followed by numerical tests in section 5. Some concluding remarks complete the study.

2. Discretization of the linear SW equations.

2.1. Governing equations. Let Ω be the model domain with boundary Γ. The inviscid linear SW equations are expressed in Cartesian coordinates [30] as

$$\bar{\mathbf{u}}_t + f\,\mathbf{k} \times \bar{\mathbf{u}} + g\,\nabla\bar{\eta} = 0\,, \tag{2.1}$$

$$\bar{\eta}_t + H\,\nabla \cdot \bar{\mathbf{u}} = 0\,, \tag{2.2}$$

where $\bar{\mathbf{u}} = (\bar{u}, \bar{v})$ is the velocity field, $\bar{\eta}$ is the surface elevation with respect to the reference level $z = 0$, g is the gravitational acceleration, $\mathbf{k}$ is a unit vector in the vertical direction, and the mean depth H and the Coriolis parameter f are assumed constant. Note that $\bar{\eta}$ would be the pressure in the Navier–Stokes equations. For a contained flow, (2.1) and (2.2) are solved subject to the no-normal flow boundary condition $\bar{\mathbf{u}} \cdot \mathbf{n} = 0$ on Γ, where $\mathbf{n}$ is the outward pointing normal at the boundary.

For this analysis we seek periodic solutions of (2.1)–(2.2) of the form

$$(2.3) \qquad \bar{\mathbf{u}}(x,y,t) = \mathbf{u}(x,y)e^{i\omega t}, \quad \bar{\eta}(x,y,t) = \eta(x,y)e^{i\omega t},$$

where $\mathbf{u} = (u,v)$, η are amplitudes, and ω is the angular frequency, and we obtain

$$(2.4) \qquad i\omega\,\mathbf{u} + f\,\mathbf{k} \times \mathbf{u} + g\,\nabla\eta = 0,$$

$$(2.5) \qquad i\omega\,\eta + H\,\nabla \cdot \mathbf{u} = 0.$$

2.2. Spatial discretization.

2.2.1. The weak formulation. We assume $\mathbf{u}$ and η belong to the spaces $\mathbf{V}$ and Q, respectively, with Q and $\mathbf{V}$ being either the square-integrable space $L^2(\Omega)$ or the Sobolev space $H^1(\Omega)$, i.e., the space of functions in $L^2(\Omega)$ whose first derivatives belong to $L^2(\Omega)$. The weak formulation of (2.4) and (2.5) requires the test functions $\boldsymbol{\varphi}$ (whose x- or y-component is formally denoted by φ) and ψ to be sufficiently regular and to belong, respectively, to the same function space as $\mathbf{u}$ and η, such that

$$(2.6) \qquad i\omega\int_\Omega \mathbf{u} \cdot \boldsymbol{\varphi}\, d\Omega + \int_\Omega f(\mathbf{k} \times \mathbf{u}) \cdot \boldsymbol{\varphi}\, d\Omega + g\int_\Omega \nabla\eta \cdot \boldsymbol{\varphi}\, d\Omega = 0,$$

$$(2.7) \qquad i\omega\int_\Omega \eta\,\psi\, d\Omega + H\int_\Omega \nabla \cdot \mathbf{u}\,\psi\, d\Omega = 0,$$

where $d\Omega$ is the area element.

Depending on the regularity of functions $\mathbf{u}$ and η, the terms containing derivatives in (2.6) and (2.7) may be integrated by parts using Green's theorem. In this way, (2.6) is rewritten if needed as

$$(2.8) \qquad i\omega\int_\Omega \mathbf{u} \cdot \boldsymbol{\varphi}\, d\Omega + \int_\Omega f(\mathbf{k} \times \mathbf{u}) \cdot \boldsymbol{\varphi}\, d\Omega - g\int_\Omega \eta\,\nabla \cdot \boldsymbol{\varphi}\, d\Omega = 0,$$

and for (2.7) we obtain

$$(2.9) \qquad i\omega\int_\Omega \eta\,\psi\, d\Omega - H\int_\Omega \mathbf{u} \cdot \nabla\psi\, d\Omega = 0,$$

by letting $\mathbf{u} \cdot \mathbf{n} = 0$ on Γ for all $\mathbf{u}$ belonging to $\mathbf{V}$. Hence, we also have $\boldsymbol{\varphi} \cdot \mathbf{n} = 0$ on Γ.

2.2.2. Galerkin FE discretization. The Galerkin method approximates the solution of (2.6) and (2.7), and eventually (2.8) and (2.9) if integration by parts needs to be performed, in finite-dimensional subspaces. Consider a FE triangulation $\mathcal{T}_h$, of the polygonal domain Ω, where h is a representative meshlength parameter that measures resolution. For triangle $K \in \mathcal{T}_h$, let $P_n(K)$ denote the space of polynomials of degree n on K.

The discrete solutions $\mathbf{u}_h$ and η_h sought belong to finite-dimensional spaces $\mathbf{V}_h$ and Q_h, respectively, whose restrictions on K belong to $P_k(K) \times P_k(K)$ for $\mathbf{u}_h$ and to $P_l(K)$ for η_h. The components of $\mathbf{u}_h$ and η_h are represented over a triangle K_i by interpolating functions $\varphi(x,y)$ of degree k and $\psi(x,y)$ of degree l (in the x- and y-components), respectively, with $\boldsymbol{\varphi}(x,y)$ belonging to $\mathbf{V}_h$ and $\psi(x,y)$ belonging to Q_h. We thus have

$$(2.10) \qquad \mathbf{u}_h = \sum_{j \in S^{\mathbf{u}}_{K_i}} \mathbf{u}_j\,\varphi_j, \quad \eta_h = \sum_{j \in S^{\eta}_{K_i}} = \eta_j\,\psi_j,$$

where j represents a node of K_i and $S_{K_i}^{\mathbf{u}}$ and $S_{K_i}^{\eta}$ denote the set of nodes of K_i.

The expansions of $\mathbf{u}_h$ and η_h over the whole domain Ω are then obtained by summing (2.10) over all triangles K_i of the triangulation $\mathcal{T}_h$. Introducing the FE basis leads to a FE statement as in (2.6) and (2.7), and eventually in (2.8) and (2.9), but with $\mathbf{u}, \eta$ replaced by the FE trial functions $\mathbf{u}_h, \eta_h$ and φ, ψ replaced by the corresponding FE test functions. We then decompose the integrals in (2.6) and (2.7) into triangle contributions.

For the purposes of the following analysis we consider a uniform mesh made up of biased right triangles as in the figures of section 3, and h is thus taken as a constant in the x- and y-directions.

2.2.3. The FE pairs. We now introduce the schemes that are used for the spatial discretization. Nine candidate FE pairs for representing velocity and surface elevation are described and evaluated in the remainder of this paper. Conventional FE terminology is adopted to describe the FE pairs. The nomenclature $P_m - P_n$ means that velocity components and surface elevation are represented, respectively, as piecewise-defined polynomials of degree m and n. Enhancements of this basic terminology are introduced as needed.

Common to the first six FE velocity/surface-elevation pairs (as shown in Figures 4.2(d) and 4.3) is a piecewise-linear continuous representation of surface elevation, and they differ from one another in their representation of velocity. The $P_1 - P_1$ pair has velocity colocated at triangle vertices, and the corresponding basis functions are piecewise-linear. The MINI element [7] also has continuous piecewise-linear basis functions at the vertices, but bubble functions are added at the barycenters for velocity in order to stabilize the pair. The $P_1^{NC} - P_1$ pair [27, 35] has velocity nodes at triangle edge midpoints, and linear basis functions are used to approximate the two velocity components on the element's two-triangle support. Since this particular representation of velocity is continuous only across triangle boundaries at midpoint nodes, and discontinuous everywhere else around a triangle boundary, this element is termed nonconforming (NC) in the FE literature. The $P_1 \,\mathrm{iso}\, P_2 - P_1$ element pair [12] has piecewise linear basis functions for velocity on a refined triangulation obtained by dividing each triangle into four subtriangles using the midpoints of triangle sides. There are thus six velocity nodes over each unrefined triangle, the same as for a quadratic approximation of velocity, termed P_2. The designation P_1 in $P_1 \,\mathrm{iso}\, P_2$ denotes linear velocity elements on subtriangles, whereas $\mathrm{iso}\, P_2$ indicates that the nodal placement is that associated with quadratic elements on unrefined triangles. The $P_2 - P_1$ pair [25], also known in the literature as the Taylor–Hood element, has quadratic velocity basis functions. Finally, the $P_0 - P_1$ pair, shown in Figure 4.2(d), has a piecewise-constant representation of velocity.

Common to the last three pairs (shown in Figures 4.2(a)–(c)) is a discontinuous piecewise-constant representation of surface elevation. The RT0 element, also called low-order Raviart–Thomas element [40], is based on flux conservation on element edges and has normal velocity components at triangle midedge points. Finally, the $P_1^{NC} - P_0$ and $P_2 - P_0$ pairs have, respectively, P_1^{NC} and P_2 representations of velocity.

3. Computation of the dispersion relations.

3.1. Matrix computations. For all FE pairs having a piecewise-constant representation of surface-elevation an integration by parts of $\nabla \eta$ in the left-hand side of (2.6) is performed, and hence (2.8) is employed. For the $P_1^{NC} - P_1$ and $P_0 - P_1$ pairs, the term $\nabla \cdot \mathbf{u}$ appearing in (2.7) is integrated by parts to avoid computing u

and v derivatives, and (2.9) is used instead.

After substitution of $\mathbf{u}_h$ and η_h from (2.10) into (2.6) and (2.7), the discrete formulation is obtained. We then need to compute

$$(3.1) \qquad M_{i,j} = \int \boldsymbol{\varphi_i} \cdot \boldsymbol{\varphi_j} \, d\Omega, \quad G_{i,j} = \int \nabla \psi_i \cdot \boldsymbol{\varphi_j} \, d\Omega, \quad D_{i,j} = \int \nabla \cdot \boldsymbol{\varphi_i} \, \psi_j \, d\Omega,$$

where $M_{i,j}, G_{i,j}$, and $D_{i,j}$ represent the mass, gradient, and divergence elementary FE matrices, respectively. When (2.8) is employed instead of (2.6) the elementary gradient matrix is then $-D_{j,i}$, and if (2.9) is used, the elementary divergence matrix becomes $-G_{j,i}$. Assembling the elementary matrices leads to the stencils of Figures 3.1, 3.2, 3.3, 3.4, and 3.5 for the pairs examined here. The symbols ● and black arrows indicate the location of velocity and normal velocity nodes, respectively. The arrow points in the direction of the chosen normal. When these symbols are represented in grey this means that velocity and normal velocities have zero values at the corresponding nodes. The symbol ○ indicates nodes for surface elevation and dotted circles mean that the elevation is zero at those nodes.

For the subsequent dispersion analysis we consider two possible types of barycenters, corresponding to lower left and upper right triangles, and three types of faces: horizontal, vertical, and diagonal. Note that for the $P_1^{NC} - P_0$ and $P_2 - P_0$ pairs in Figure 3.2, the x- (resp., y-) component of the surface elevation gradient is zero on horizontal (resp., vertical) faces. Further, in Figure 3.4 for the $P_2 - P_1$ pair, the surface-elevation gradient is zero at vertex nodes.

3.2. The continuous case. The free modes of (2.4)–(2.5) are examined by perturbing about the basic state $u = v = \eta = 0$. Because the governing equations are linear, the solution may be examined by considering the behavior of one Fourier mode. We then seek solutions of (2.4)–(2.5) of the form $(u, v, \eta) = (\tilde{u}, \tilde{v}, \tilde{\eta}) \, e^{i(kx+ly)}$, where k and l are the wave numbers in the x- and y-directions, respectively. Substitution into (2.4)–(2.5) leads to a square matrix system for the amplitudes $\tilde{u}, \tilde{v}, \tilde{\eta}$. For a nontrivial solution to exist, the determinant of the matrix must equal zero, and this constraint leads to a relationship between the two wave numbers k and l and the frequency ω. The so-called dispersion relation is then obtained for the frequency

$$(3.2) \qquad \omega \, (\, \omega^2 - f^2 - g \, H \, (\, k^2 + l^2 \,) \,) = 0 \, .$$

The first solution $\omega = 0$ is the geostrophic mode, and it would correspond to the slow Rossby mode on a β-plane, while the other two solutions

$$(3.3) \qquad \omega_{AN} = \pm \sqrt{f^2 + g \, H \, (\, k^2 + l^2 \,)}$$

correspond to the free-surface gravitational modes with rotational correction. Since ω is purely real, all modes are neutrally stable and neither amplify nor decay.

3.3. The discrete case. For each FE pair, the discrete momentum and continuity equations are obtained from the stencils of Figures 3.1, 3.2, 3.3, 3.4, and 3.5. As previously mentioned, the following analysis will consider a uniform mesh made up of biased right triangles as in the figures of section 3, and h is thus taken as a constant in the x- and y-directions. Because nodal unknowns may be located on different types of nodes, i.e., vertices, faces, and barycenters, selected discrete equations for each type of node are retained. For example, the $P_2 - P_1$ pair leads to considering four discrete momentum equations, one at a typical vertex node and three on the three possible
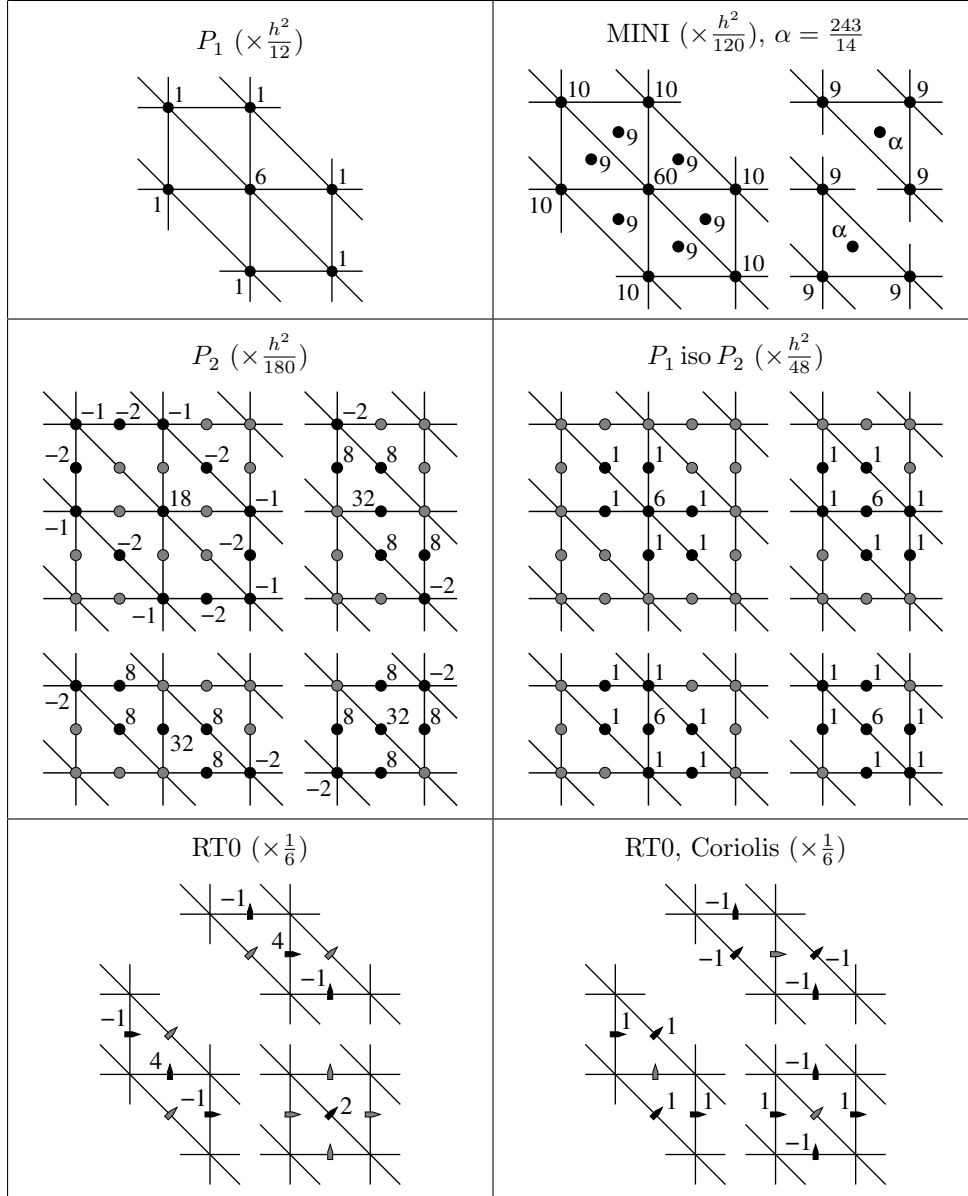
FIG. 3.1. *Mass stencils for several FE discretizations. The symbols ● and black arrows indicate the location of velocity and normal velocity nodes, respectively. The arrow points in the direction of the chosen normal. Grey symbols mean that velocity and normal velocities have zero values at the corresponding nodes.*

types of faces, i.e., horizontal, vertical, and diagonal (written as H, V, and D, respectively, in the following), and only one discrete continuity equation at a typical vertex node (written as S in the following). For the $P_0 - P_1$ pair, two discrete momentum equations are retained at the two possible types of barycenters (corresponding to lower left and upper right triangles, written as C_1 and C_2, respectively, in the following). More details are given in [10, 21] for the $P_1 - P_1$ pair, and in [35] for the $P_1^{NC} - P_1$
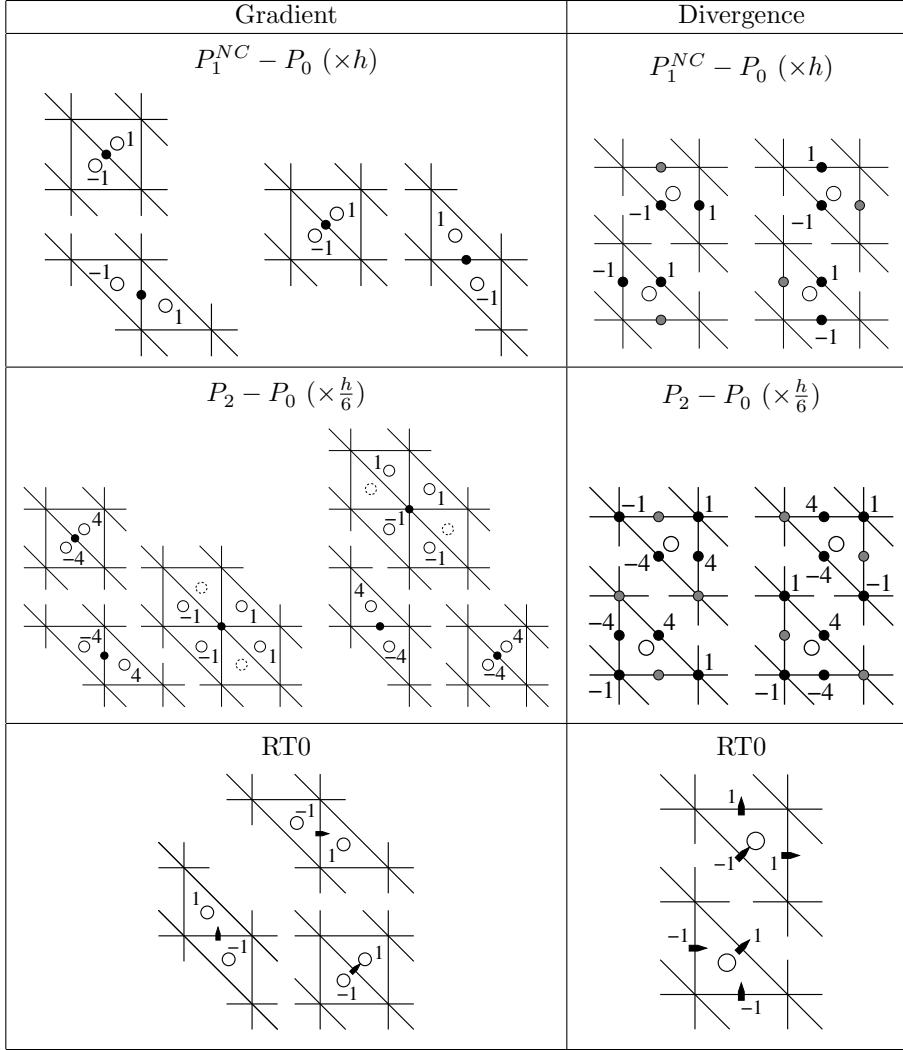
FIG. 3.2. *As for Figure* 3.1 *but for the gradient and divergence stencils of the* $P_1^{NC} - P_0$, $P_2 - P_0$, *and* RT0 *pairs. For the* $P_1^{NC} - P_0$ *and* $P_2 - P_0$ *pairs, the* x- *and* y-*components are on the left and right sides, respectively. The symbol* $\bigcirc$ *indicates nodes for surface elevation and dotted circles mean that the elevation is zero at those nodes.*

one, to compute their dispersion relations. For all pairs, the typical nodes belonging to the same set (vertices, faces, midedge points, or barycenters) are hence distributed on a regular grid of size h.

As for the continuum case, the dispersion relation for the discrete scheme is found through a Fourier expansion. The discrete solutions corresponding to $(u_j, v_j, \eta_j) = (\tilde{u}, \tilde{v}, \tilde{\eta}) \, e^{i(kx_j + ly_j)}$ are sought at node j ($j = 1, 2, 3 \ldots$), where (u_j, v_j, η_j) are the nodal unknowns that appear in the selected discrete equations and $(\tilde{u}, \tilde{v}, \tilde{\eta})$ are amplitudes. The (x_j, y_j) coordinates are expressed in terms of a distance to a reference node. Substitution into the discrete equations leads to a square matrix system for the Fourier amplitudes. The dispersion relation is then obtained by setting the determinant of the matrix system to zero.

Gradient	Divergence
$P_0 - P_1 \ (\times \frac{h}{2})$	$P_0 - P_1 \ (\times \frac{h}{2})$
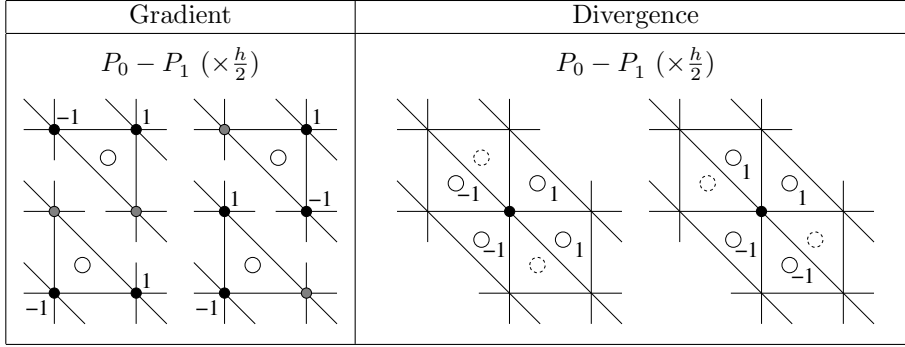
FIG. 3.3. *As for Figure* 3.2 *but for the* $P_0 - P_1$ *pair.*

We let I_n be the $n \times n$ identity matrix, M an $m \times n$ matrix with m and n two positive integers, and $M^* = \overline{M}^T$ the conjugate transpose of M, and we define

$$a = \frac{1}{3}(3 + \cos kh + \cos lh + \cos(k-l)h), \quad A = \begin{pmatrix} i\omega & -f \\ f & i\omega \end{pmatrix},$$

with $a \geq \frac{1}{2}$ for all k and l.

We now examine the dispersion relations corresponding to the nine pairs that are considered in this study.

3.4. The $P_1^{NC} - P_0$ pair. The selected discrete equations are written in the matrix form

(3.4)
$$\begin{pmatrix} A & 0 & 0 & \\ 0 & A & 0 & -g\,B^* \\ 0 & 0 & A & \\ & HB & & \frac{3}{2}i\omega I_2 \end{pmatrix} \begin{pmatrix} \tilde{\mathbf{u}}_H \\ \tilde{\mathbf{u}}_V \\ \tilde{\mathbf{u}}_D \\ \tilde{\boldsymbol{\eta}} \end{pmatrix} = 0,$$

where $\tilde{\boldsymbol{\eta}} = (\tilde{\eta}_{C_1}, \tilde{\eta}_{C_2})$, and

$$B = \frac{3}{h}\begin{pmatrix} 0 & -b_1 & -\bar{b}_3 & 0 & b_2 & b_2 \\ 0 & \bar{b}_1 & b_3 & 0 & -\bar{b}_2 & -\bar{b}_2 \end{pmatrix},$$

with

$$b_1 = e^{i(k-2l)\frac{h}{6}}, \quad b_2 = e^{i(k+l)\frac{h}{6}}, \quad b_3 = e^{i(2k-l)\frac{h}{6}}.$$

Vanishing the above 8×8 determinant leads to

$$\omega_{1,2} = 0, \quad \omega_{3,4} = \pm f, \quad \omega_{5,6} = \pm\sqrt{f^2 + 6\frac{gH}{h^2}(4-\alpha)}, \quad \omega_{7,8} = \pm\sqrt{f^2 + 6\frac{gH}{h^2}(4+\alpha)},$$

with $\alpha = \sqrt{2(3a + \cos kh + \cos lh)}$. For infinitesimal mesh spacing we obtain

(3.5)
$$\omega_{5,6} = \pm\sqrt{f^2 + gH\left(\frac{9}{4}(k^2 + l^2) - \frac{3}{2}kl\right)} + O(h^2),$$

(3.6)
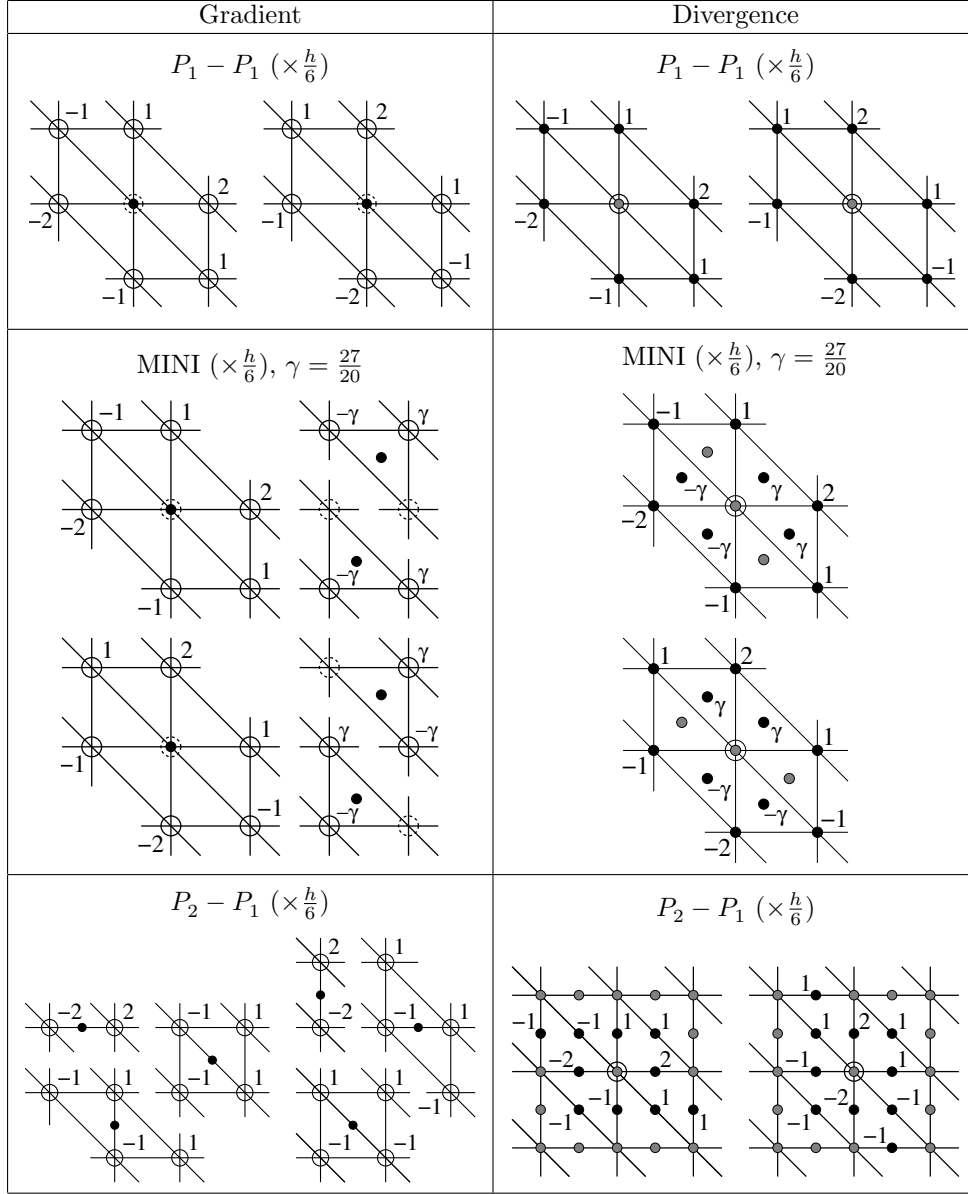$$\omega_{7,8} = \pm 4\sqrt{3}\frac{\sqrt{gH}}{h} + O(h).$$

FIG. 3.4. *As for Figure* 3.2 *but for the* $P_1 - P_1$, *MINI and* $P_2 - P_1$ *pairs. For the* $P_1 - P_1$ *and* $P_2 - P_1$ *pairs, the x- and y-components are on the left and right sides, respectively, and they are at the top and bottom, respectively, for MINI.*

Note that neither $\omega_{5,6}$ nor $\omega_{7,8}$ coincide with the continuous solution obtained from (3.2) in the limit as mesh spacing $h \to 0$. The roots $\omega_{7,8}$ correspond to a spurious mode from the $P_1^{NC} - P_0$ discretization scheme. Such a mode of type $O(\frac{1}{h})$ has already been observed in [34], where the one-dimensional SW equations are discretized using the discontinuous Galerkin method. Finally, the roots $\omega_{3,4}$ represent spurious inertial oscillations. It has been shown in [1] for the FD CD-grid and in [35] for the $P_1^{NC} - P_1$ pair that such spurious modes take the form of propagating inertial oscillations and
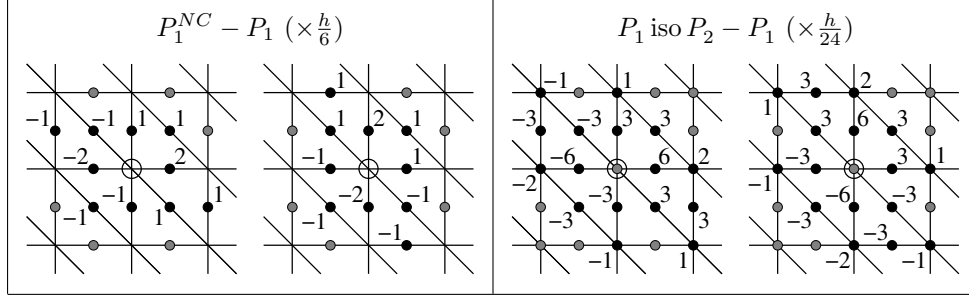
FIG. 3.5. *Divergence stencils for the $P_1^{NC} - P_1$ and P_1 iso $P_2 - P_1$ pairs. For each pair, the x- and y-components are on the left and right sides, respectively.*

have no particular spatial characteristics. They are a consequence of using more velocity nodes than surface-elevation nodes.

3.5. The $P_2 - P_0$ pair. The selected discrete equations lead to

$$(3.7) \qquad \begin{pmatrix} a_1 A & a_3 A & a_4 A & a_2 A & \\ a_3 A & a_8 A & a_7 A & a_6 A & \\ & & & & -gB^* \\ a_4 A & a_7 A & a_8 A & a_5 A & \\ a_2 A & a_6 A & a_5 A & a_8 A & \\ & & HB & & \frac{i\omega}{2} I_2 \end{pmatrix} \begin{pmatrix} \tilde{\mathbf{u}}_S \\ \tilde{\mathbf{u}}_H \\ \tilde{\mathbf{u}}_V \\ \tilde{\mathbf{u}}_D \\ \tilde{\boldsymbol{\eta}} \end{pmatrix} = 0,$$

where $\tilde{\boldsymbol{\eta}} = (\tilde{\eta}_{C_1}, \tilde{\eta}_{C_2})$,

$$B = \frac{1}{6h} \begin{pmatrix} -\bar{b}_1 + \bar{b}_2 & -\bar{b}_1 + \bar{b}_5 & 0 & -4\bar{b}_6 & -4\bar{b}_4 & 0 & 4\bar{b}_3 & 4\bar{b}_3 \\ b_1 - b_2 & b_1 - b_5 & 0 & 4b_6 & 4b_4 & 0 & -4b_3 & -4b_3 \end{pmatrix},$$

with $a_1 = \frac{1}{30}(4 - a)$, $a_8 = \frac{8}{45}$, and

$$a_2 = -\frac{1}{45} \cos \frac{(k+l)h}{2}, \qquad a_5 = \frac{4}{45} \cos \frac{kh}{2}, \qquad b_1 = e^{i(k+l)\frac{h}{3}}, \qquad b_4 = e^{i(2k-l)\frac{h}{6}},$$

$$a_3 = -\frac{1}{45} \cos(\frac{k-2l}{2})h, \quad a_6 = \frac{4}{45} \cos \frac{lh}{2}, \qquad b_2 = e^{-i(2k-l)\frac{h}{3}}, \quad b_5 = e^{i(k-2l)\frac{h}{3}},$$

$$a_4 = -\frac{1}{45} \cos \frac{(2k-l)h}{2}, \quad a_7 = \frac{4}{45} \cos \frac{(k-l)h}{2}, \quad b_3 = e^{-i(k+l)\frac{h}{6}}, \quad b_6 = e^{-i(k-2l)\frac{h}{6}}.$$

Vanishing the above 10×10 determinant leads to a polynomial in ω of the form

$$(\omega^2 - f^2)^2 \left(c_6 \omega^6 + c_4 \omega^4 + c_2 \omega^2 + c_0 \right) = 0,$$

where $c_0, c_2, c_4,$ and c_6 are functions of k and l. We then obtain

$$\omega_{1,2} = \pm O(h), \quad \omega_{3,4,5,6} = \pm f \text{ (double root)}, \quad \omega_{7,8} = \pm O(1), \quad \omega_{9,10} = \pm O\left(\frac{1}{h}\right).$$

We have found that $c_0 \neq 0$, and hence $\omega = 0$ is no longer a solution to the dispersion relation, and the possibility of damped or growing slow modes occurs. However, we note the appearance of modes $\omega_{1,2} = \pm O(h)$ which are expected to be close to zero in the limit as mesh spacing $h \to 0$. As for the $P_1^{NC} - P_0$ pair, the roots $\omega_{3,4,5,6}$ represent

spurious inertial oscillations. They are again due to an imbalance in the number of degrees of freedom between velocity and surface-elevation nodes. We have also found, as for the $P_1^{NC} - P_0$ pair, that the frequencies corresponding to inertia-gravity modes, here $\omega_{7,8}$, do not coincide with the continuous solution obtained from (3.2) in the limit as mesh spacing $h \to 0$. Finally, the frequencies $\omega_{9,10}$ again correspond to a spurious mode from the $P_2 - P_0$ discretization scheme, as for the $P_1^{NC} - P_0$ pair.

3.6. The RT0 pair. The discrete equations lead to the following system:

$$(3.8) \qquad \begin{pmatrix} A_{\mathrm{RT0}} & -g\,B^* \\ HB & i\omega\frac{h^2}{2}I_2 \end{pmatrix} \begin{pmatrix} \tilde{\mathbf{J}} \\ \tilde{\boldsymbol{\eta}} \end{pmatrix} = 0,$$

where $\tilde{\mathbf{J}} = (\tilde{J}_H, \tilde{J}_D, \tilde{J}_V)$ and J_p is the velocity flux through the edge containing node p (here $H, D,$ or V), with $J_p = \tilde{J}_p\, e^{i(kx_p + ly_p)}$. We also have $\tilde{\boldsymbol{\eta}} = (\tilde{\eta}_{C_1}, \tilde{\eta}_{C_2})$,

$$A_{\mathrm{RT0}} = \frac{1}{3} \begin{pmatrix} 2i\omega & a_2 f & -a_3(i\omega - f) \\ -a_2 f & i\omega & a_1 f \\ -a_3(i\omega + f) & -a_1 f & 2i\omega \end{pmatrix}, \quad B = \begin{pmatrix} -b_1 & b_2 & -b_3 \\ \bar{b}_1 & -\bar{b}_2 & \bar{b}_3 \end{pmatrix},$$

and

$$a_1 = \cos\tfrac{kh}{2}, \qquad a_2 = \cos\tfrac{lh}{2}, \qquad a_3 = \cos\tfrac{(k-l)h}{2},$$
$$b_1 = e^{i(k-2l)\frac{h}{6}}, \quad b_2 = e^{i(k+l)\frac{h}{6}}, \quad b_3 = e^{-i(2k-l)\frac{h}{6}}.$$

For the 5×5 determinant to vanish we obtain $\omega = 0$ and four additional roots corresponding to gravity modes. For infinitesimal mesh spacing we have

$$\omega_1 = 0, \quad \omega_{2,3} = \omega_{AN} + O(h^2), \quad \omega_{4,5} = \pm 6\frac{\sqrt{gH}}{h} + O(h).$$

Note that only $\omega_{2,3}$ coincide with the continuous solution obtained from (3.2) in the limit as mesh spacing $h \to 0$, while $\omega_{4,5}$ presumably correspond to spurious modes from the RT0 discretization scheme.

3.7. The $P_0 - P_1$ pair. The selected discrete equations are written in the matrix form

$$(3.9) \qquad \begin{pmatrix} A & 0 & \\ 0 & A & -gB^* \\ & HB & ia\omega \end{pmatrix} \begin{pmatrix} \tilde{\mathbf{u}}_{C_1} \\ \tilde{\mathbf{u}}_{C_2} \\ \tilde{\eta}_S \end{pmatrix} = 0,$$

where $B = \frac{1}{h}\begin{pmatrix} b_1 & b_2 & -\bar{b}_1 & -\bar{b}_2 \end{pmatrix}$, with

$$b_1 = e^{i(k+l)\frac{h}{3}}(1 - e^{-ikh}), \quad b_2 = e^{i(k+l)\frac{h}{3}}(1 - e^{-ilh}).$$

Vanishing the above 5×5 determinant leads to

$$\omega_1 = 0, \quad \omega_{2,3} = \pm f, \quad \omega_{4,5} = \pm\sqrt{f^2 + 4\frac{gH}{h^2}\left(\frac{2 - \cos kh - \cos lh}{a}\right)}.$$

For infinitesimal mesh spacing the frequencies $\omega_{4,5}$ coincide with the continuous solution obtained from (3.2) in the limit as mesh spacing $h \to 0$, and we have $\omega_{4,5} = \omega_{AN} + O(h^2)$. Again, the roots $\omega_{2,3}$ represent spurious inertial oscillations.

3.8. The $P_1 - P_1$ pair. The selected discrete equations lead to

$$(3.10) \qquad \begin{pmatrix} aA & -g\,B^* \\ H\,B & ia\omega \end{pmatrix} \begin{pmatrix} \tilde{\mathbf{u}}_S \\ \tilde{\eta}_S \end{pmatrix} = 0,$$

where $B = \frac{2i}{3h} \begin{pmatrix} b_1 & b_2 \end{pmatrix}$, with

$$b_1 = 2\sin kh + \sin lh + \sin(k-l)h, \quad b_2 = \sin kh + 2\sin lh - \sin(k-l)h.$$

For a nontrivial solution to exist, the 3×3 determinant of the coefficient matrix above must vanish. This condition implies

$$\omega_1 = 0, \quad \omega_{2,3} = \pm\sqrt{f^2 + \frac{4}{9}\frac{gH}{h^2}\frac{(b_1^2 + b_2^2)}{a^2}}.$$

For infinitesimal mesh spacing we obtain $\omega_{2,3} = \omega_{AN} + O(h^4)$. In the case $f = 0$, corresponding to the propagation of pure gravity waves, we may have $\omega_{2,3} = 0$ if $b_1 = b_2 = 0$. This occurs, in particular, when $kh = lh = \pi$ (wavelength $2h$) or when $kh = -lh = \frac{2\pi}{3}$ (wavelength $3h$). The waves of length $2h$ and $3h$ hence lead to $\omega_{2,3} = 0$ and do not propagate, but they are trapped within the model grid. They are numerical artifacts introduced by the spatial discretization scheme and describe oscillations of wavelength $2h$ and $3h$. Such waves are identified as spurious surface-elevation modes corresponding to physical eigenmodes which have their phase speed reduced to zero by the numerical scheme and appear as stationary oscillations [45, 21]. They can cause an accumulation of energy in the smallest-resolvable scale, leading to noisy solutions.

3.9. The MINI pair. If a cubic bubble is employed, the discrete equations lead to the following system:

$$(3.11) \qquad \begin{pmatrix} aA & \bar{a}_1 A & a_1 A & \\ a_1 A & a_2 A & 0 & -g\,B^* \\ \bar{a}_1 A & 0 & a_2 A & \\ & H\,B & & ia\omega \end{pmatrix} \begin{pmatrix} \tilde{\mathbf{u}}_S \\ \tilde{\mathbf{u}}_{C_1} \\ \tilde{\mathbf{u}}_{C_2} \\ \tilde{\eta}_S \end{pmatrix} = 0,$$

where $B = \frac{1}{h} \begin{pmatrix} b_1 & b_2 & b_3 & b_4 & -\bar{b}_3 & -\bar{b}_4 \end{pmatrix}$, with

$$a_1 = \frac{3}{20}e^{i(k+l)\frac{h}{6}}\left(2\cos\frac{(k-l)h}{2} + e^{\frac{-i}{2}(k+l)h}\right), \quad a_2 = \frac{81}{280},$$

$$b_1 = \frac{2i}{3}(2\sin kh + \sin lh + \sin(k-l)h), \qquad b_2 = \frac{2i}{3}(2\sin lh + \sin kh + \sin(l-k)h),$$

$$b_3 = \frac{9}{20}e^{i(k+l)\frac{h}{3}}(1 - e^{-ikh}), \qquad b_4 = \frac{9}{20}e^{i(k+l)\frac{h}{3}}(1 - e^{-ilh}).$$

For the 7×7 determinant to vanish we obtain

$$\omega_1 = 0, \quad \omega_{2,3,4,5} = \pm f \text{ (double root)}, \quad \omega_{6,7} = O(1).$$

For infinitesimal mesh spacing we have $\omega_{6,7} = \omega_{AN} + O(h^2)$, and the roots $\omega_{2,3,4,5}$ represent spurious inertial oscillations.

The MINI discretization offers the particularity that equations associated with bubble nodes on an element depend only on the values of the solution on that element. This permits us to eliminate the bubble unknowns at the element level through a

procedure called static condensation [22]. The linear system (3.11) reduces to a 3×3 one after static condensation, and for the corresponding 3×3 determinant to vanish we exactly obtain the solutions ω_1 and $\omega_{6,7}$. Because the factor $(\omega^2 - f^2)^{-2}$ arises during the procedure, the solutions $\omega_{2,3,4,5}$ also need to be considered. Finally, we have also performed the calculations and numerical experiments with a linear bubble, instead of a cubic one, and insignificant differences have been observed.

3.10. The $P_1^{NC} - P_1$ pair. The selected discrete equations are written in the matrix form

(3.12)
$$
\begin{pmatrix}
A & 0 & 0 & \\
0 & A & 0 & -g\,B^* \\
0 & 0 & A & \\
 & HB & & \frac{3}{2}ia\omega
\end{pmatrix}
\begin{pmatrix}
\tilde{\mathbf{u}}_H \\
\tilde{\mathbf{u}}_V \\
\tilde{\mathbf{u}}_D \\
\tilde{\eta}_S
\end{pmatrix} = 0,
$$

where $B = \frac{1}{h}\left(\begin{array}{cccccc} b_1 & b_2 & b_3 & b_4 & b_5 & b_6 \end{array}\right)$, with

$$b_1 = 2i\sin\tfrac{kh}{2}, \quad b_2 = 2i\sin\tfrac{lh}{2}\,\cos\tfrac{(k-l)h}{2}, \quad b_3 = 2i\sin\tfrac{kh}{2}\,\cos\tfrac{(k-l)h}{2},$$
$$b_4 = 2i\sin\tfrac{lh}{2}, \quad b_5 = 2i\sin\tfrac{kh}{2}\,\cos\tfrac{lh}{2}, \qquad b_6 = 2i\sin\tfrac{lh}{2}\,\cos\tfrac{kh}{2}.$$

Vanishing the above 7×7 determinant leads to

$$\omega_1 = 0, \quad \omega_{2,3,4,5} = \pm f \ \text{(double root)}, \quad \omega_{6,7} = \pm\sqrt{f^2 + 4\frac{gH}{h^2}\alpha},$$

with

$$\alpha = \sin^2\frac{kh}{2} + \sin^2\frac{lh}{2} + \frac{2}{3a}\left[\sin^4\frac{kh}{2} + \sin^4\frac{lh}{2}\right].$$

The above frequencies coincide with those found in [35], where temporally discretized SW equations are considered, in the limit as time step $\Delta t \to 0$. For infinitesimal mesh spacing we obtain $\omega_{6,7} = \omega_{AN} + O(h^4)$.

3.11. The $P_1\,\mathrm{iso}\,P_2 - P_1$ pair. The selected discrete equations lead to

(3.13)
$$
\begin{pmatrix}
3A & a_1A & a_2A & a_3A & \\
a_1A & 3A & a_3A & a_2A & \\
 & & & & -gB^* \\
a_2A & a_3A & 3A & a_1A & \\
a_3A & a_2A & a_1A & 3A & \\
 & & HB & & 12ia\omega
\end{pmatrix}
\begin{pmatrix}
\tilde{\mathbf{u}}_S \\
\tilde{\mathbf{u}}_H \\
\tilde{\mathbf{u}}_V \\
\tilde{\mathbf{u}}_D \\
\tilde{\eta}_S
\end{pmatrix} = 0,
$$

where $B = \frac{1}{h}\left(\begin{array}{cccccccc} b_1 & b_2 & b_3 & b_4 & b_5 & b_6 & b_7 & b_8 \end{array}\right)$, with

$$a_1 = \cos\tfrac{kh}{2}, \quad a_2 = \cos\tfrac{lh}{2}, \quad a_3 = \cos\tfrac{(k-l)h}{2}, \quad b_4 = 6i(\sin\tfrac{kh}{2} - \sin\tfrac{(k-2l)h}{2}),$$
$$b_1 = 2i(2\sin kh + \sin lh + \sin(k-l)h), \qquad b_5 = 6i(\sin\tfrac{lh}{2} + \sin\tfrac{(2k-l)h}{2}),$$
$$b_2 = 2i(2\sin lh + \sin kh - \sin(k-l)h), \qquad b_7 = 6i(\sin\tfrac{(k-l)h}{2} + \sin\tfrac{(k+l)h}{2}),$$
$$b_3 = 12i\sin\tfrac{kh}{2}, \quad b_6 = 12i\sin\tfrac{lh}{2}, \qquad b_8 = 6i(\sin\tfrac{(k+l)h}{2} - \sin\tfrac{(k-l)h}{2}).$$

For the 9×9 determinant to vanish we obtain

$$\omega_1 = 0, \quad \omega_{2,3,4,5,6,7} = \pm f \ \text{(triple root)}, \quad \omega_{8,9} = O(1).$$

For infinitesimal mesh spacing we have $\omega_{8,9} = \omega_{AN} + O(h^2)$.

3.12. The $P_2 - P_1$ pair. The discrete equations lead to the following system:

$$(3.14) \quad \left(\begin{array}{ccccc} a_1A & a_4A & a_5A & a_3A & \\ a_4A & a_2A & a_8A & a_7A & \\ & & & & -gB^* \\ a_5A & a_8A & a_2A & a_6A & \\ a_3A & a_7A & a_6A & a_2A & \\ & & HB & & \frac{1}{2}ia\omega \end{array} \right) \left(\begin{array}{c} \tilde{\mathbf{u}}_S \\ \tilde{\mathbf{u}}_H \\ \tilde{\mathbf{u}}_V \\ \tilde{\mathbf{u}}_D \\ \tilde{\eta}_S \end{array} \right) = 0,$$

where $B = \frac{1}{h} \left(\begin{array}{cccccccc} 0 & 0 & b_1 & b_2 & b_3 & b_4 & b_5 & b_6 \end{array} \right)$, with $a_1 = \frac{1}{30}(4 - a)$, $a_2 = \frac{8}{45}$, and

$$a_3 = \frac{-1}{45} \cos \frac{(k+l)h}{2}, \quad a_4 = \frac{-1}{45} \cos \frac{(k-2l)h}{2}, \quad a_5 = \frac{-1}{45} \cos \frac{(2k-l)h}{2},$$

$$a_6 = \frac{4}{45} \cos \frac{kh}{2}, \quad a_7 = \frac{4}{45} \cos \frac{lh}{2}, \quad a_8 = \frac{4}{45} \cos \frac{(k-l)h}{2},$$

$$b_1 = \frac{2i}{3} \sin \frac{kh}{2}, \quad b_2 = \frac{2i}{3} \sin \frac{lh}{2} \cos \frac{(k-l)h}{2}, \quad b_3 = \frac{2i}{3} \sin \frac{kh}{2} \cos \frac{(k-l)h}{2},$$

$$b_4 = \frac{2i}{3} \sin \frac{lh}{2}, \quad b_5 = \frac{2i}{3} \sin \frac{kh}{2} \cos \frac{lh}{2}, \quad b_6 = \frac{2i}{3} \sin \frac{lh}{2} \cos \frac{kh}{2}.$$

Vanishing the above 9×9 determinant leads to

$$\omega_1 = 0, \quad \omega_{2,3,4,5,6,7} = \pm f \text{ (triple root)}, \quad \omega_{8,9} = O(1).$$

For infinitesimal mesh spacing we obtain $\omega_{8,9} = \omega_{AN} + O(h^2)$.

3.13. Summary of discrete frequencies. The previous results are summarized in Table 3.1, where n is the degree of the dispersion relation, and hence the total number of discrete frequencies, for the nine FE schemes examined in section 3.

TABLE 3.1
Number of frequencies of type $\omega = 0$, $O(1)$, $O(\frac{1}{h})$, $O(h)$, $\pm f$, solutions of the dispersion relation of degree n for the nine FE schemes examined in section 3.

FE pair	n	$\omega = 0$	$O(1)$	$O(1) \rightarrow \omega_{AN}$ when $h \rightarrow 0$	$O(\frac{1}{h})$	$O(h)$	f	$-f$
$P_1^{NC} - P_0$	8	2	2	no	2	0	1	1
$P_2 - P_0$	10	0	2	no	2	2	2	2
RT0	5	1	2	yes	2	0	0	0
$P_0 - P_1$	5	1	2	yes	0	0	1	1
$P_1 - P_1$	3	1	2	yes	0	0	0	0
MINI	7	1	2	yes	0	0	2	2
$P_1^{NC} - P_1$	7	1	2	yes	0	0	2	2
P_1 iso $P_2 - P_1$	9	1	2	yes	0	0	3	3
$P_2 - P_1$	9	1	2	yes	0	0	3	3

We mention whether frequencies of type $O(1)$, corresponding to inertia-gravity modes, coincide with the analytical solution ω_{AN} in the limit as mesh parameter $h \rightarrow 0$. This is the case for all FE pairs, except for the $P_1^{NC} - P_0$ and $P_2 - P_0$ schemes, i.e., when n is even. We also notice the presence of spurious frequencies of type $O(\frac{1}{h})$ for the $P_1^{NC} - P_0$, $P_2 - P_0$, and RT0 pairs, i.e., when a piecewise-constant representation of the surface elevation is employed. Such solutions have already been observed in [34], where the one-dimensional SW equations are discretized using the discontinuous Galerkin method. The slow mode corresponding to $\omega = 0$ is not present

for the $P_2 - P_0$ pair; however, a mode of type $O(h)$ appears instead, while $\omega = 0$ is a double root for the $P_1^{NC} - P_0$ pair. Finally, the solutions $\pm f$ are propagating spurious inertial oscillations that have no particular spatial characteristics. They are a consequence of using more velocity nodes than surface-elevation nodes [35] and are present for all schemes except for the $P_1 - P_1$ and RT0 pairs.

4. Analysis of the dispersion relations. We now analyze the computed frequencies obtained from the dispersion relations for the nine FE pairs examined in section 3. We first consider the gravity wave limit, where $f = 0$, and will then comment on the cases $f \neq 0$ and other modes.

4.1. Gravity wave limit. We let $f = 0$, and examine the computed frequencies, denoted by ω_{CP}, corresponding to pure gravity modes of type $O(1)$, as functions of kh and lh. From (3.3) and the results of section 3, we determine the analytical and computed phase speeds, denoted by c_{AN} and c_{CP}, respectively,

$$c_{AN} \equiv \frac{\omega_{AN}}{\sqrt{k^2 + l^2}} = \pm\sqrt{gH}, \quad c_{CP} \equiv \frac{\omega_{CP}}{\sqrt{k^2 + l^2}}.$$

We then obtain the phase speed ratio of the computed phase speed to the analytical one, denoted by r_{PH}, with

(4.1)
$$r_{PH} \equiv \frac{|c_{CP}|}{|c_{AN}|} = \frac{|\omega_{CP}|}{|\omega_{AN}|} = \frac{|\omega_{CP}|}{\sqrt{gH(k^2 + l^2)}}.$$

Note that we should have $r_{PH} = 1$ in the absence of numerical dispersion. We show r_{PH} as a surface function depending on kh and lh, and along the selected axes OX, OY, OD1, and OD2 (vertical section), in Figures 4.2 and 4.3, respectively, for the FE schemes previously examined. As in [21], the values of kh and lh vary over their complete domain $[-\pi, \pi]$. However, the phase speed ratio along selected axes is plotted only on $[0, \pi]$, and the solution is then deduced on $[-\pi, 0]$ by symmetry through the origin. The directions OX, OY, OD1, and OD2 are shown in Figure 4.1.
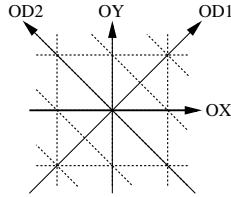

FIG. 4.1. *Definition of the directions OX, OY, OD1, and OD2 on a uniform mesh made up of biased right triangles.*

The directions OX and OY correspond to waves travelling in the x- and y-directions, for $lh = 0$ and $kh = 0$, respectively, while the directions OD1 and OD2 correspond to waves travelling along the diagonal axes, for $kh = lh$ and $lh = -kh$, respectively.

For the $P_1^{NC} - P_0$ and $P_2 - P_0$ pairs in Figure 4.2, r_{PH} is unexpectedly greater than 1 for small values of $|kh|$ and $|lh|$. Indeed, depending on the direction the wave numbers tend to zero, the phase speed ratio ranges from 1.2 to 1.7 for the $P_1^{NC} - P_0$ pair and from 1.8 to 2.5 for the $P_2 - P_0$ one. We notice that for both pairs r_{PH} decreases for increasing values of $|kh|$ and $|lh|$, implying that gravity modes propagate
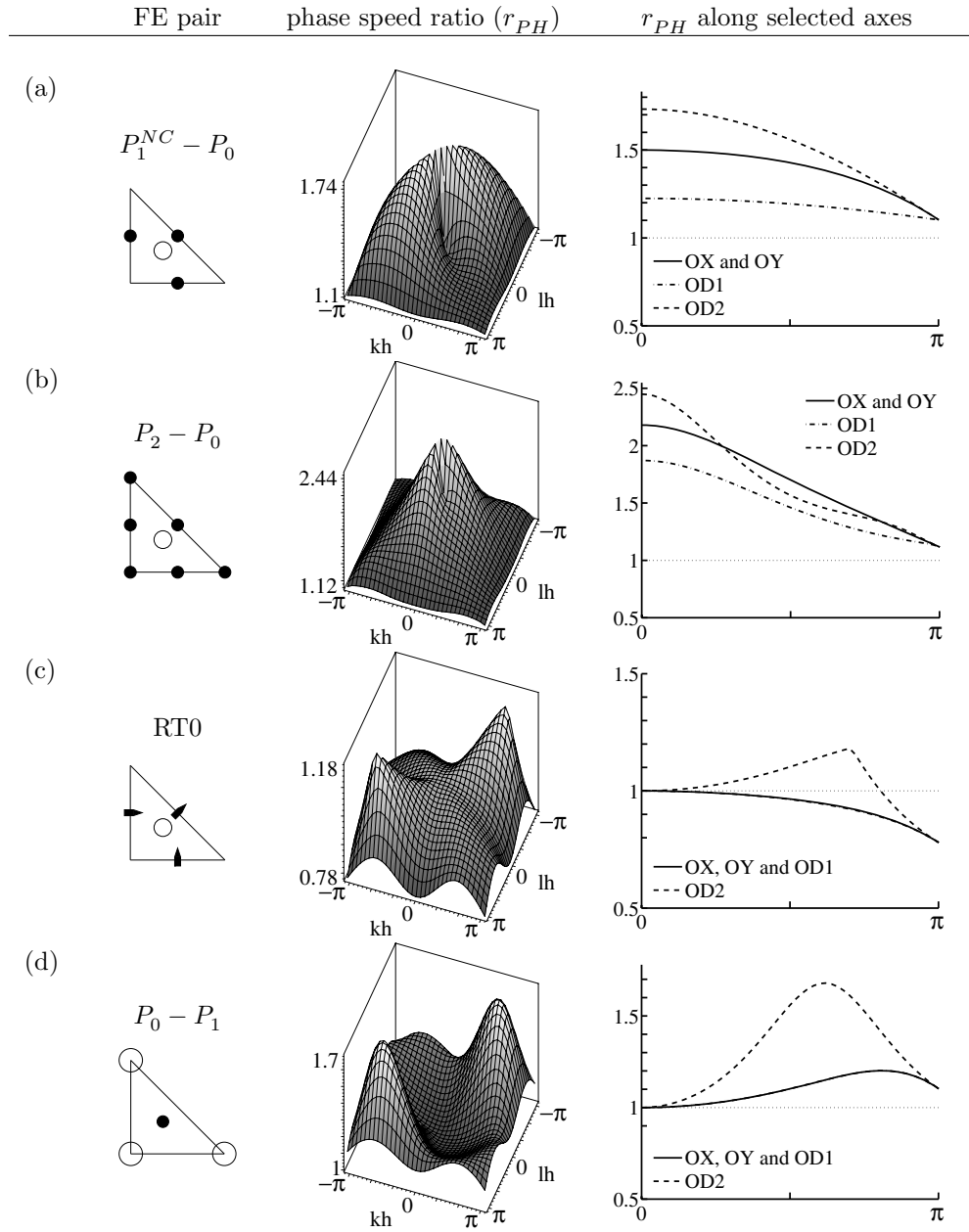
FE pair	phase speed ratio (r_{PH})	r_{PH} along selected axes

(a)

$P_1^{NC} - P_0$

(b)

$P_2 - P_0$

(c)

RT0

(d)

$P_0 - P_1$

FIG. 4.2. *The phase speed ratio is plotted as a surface function and along selected axes (OX, OY, OD1, and OD2) for the* (a) $P_1^{NC} - P_0$, (b) $P_2 - P_0$, (c) RT0, *and* (d) $P_0 - P_1$ *pairs.*

more rapidly for small wave numbers. Consequently, both pairs poorly represent the propagation of pure gravity waves.

For the $P_1 - P_1$ pair in Figure 4.3, we obtain $r_{PH} \leq 1$ for all values of kh and lh. Hence, the waves are travelling slower than expected, and this is particularly true for large values of $|kh|$ and $|lh|$. We have $r_{PH} = 0$ in the OX, OY, and OD1 directions at the following values of (kh, lh), $(0, \pm\pi)$, $(\pm\pi, 0)$, $(\pm\pi, \pm\pi)$ (waves of length $2h$),
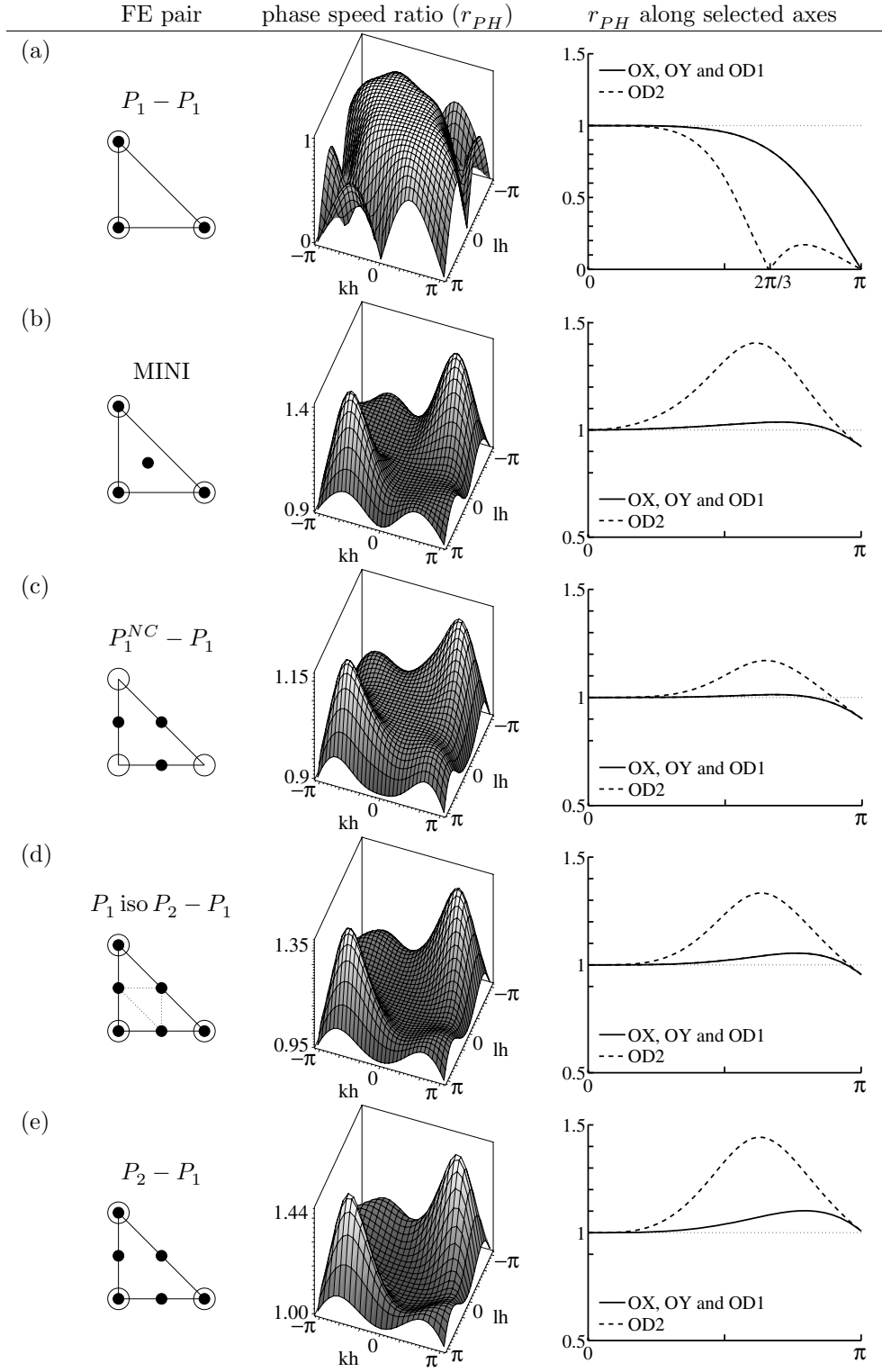
FE pair	phase speed ratio (r_{PH})	r_{PH} along selected axes

(a)

$P_1 - P_1$

(b)

MINI

(c)

$P_1^{NC} - P_1$

(d)

$P_1 \operatorname{iso} P_2 - P_1$

(e)

$P_2 - P_1$

FIG. 4.3. *As for Figure* 4.2 *but for the* (a) $P_1 - P_1$, (b) *MINI,* (c) $P_1^{NC} - P_1$, (d) $P_1 \operatorname{iso} P_2 - P_1$, *and* (e) $P_2 - P_1$ *pairs.*

and also in the OD2 direction for $|kh| = |lh| = \frac{2\pi}{3}$ (waves of length $3h$). This is a consequence of having zero frequency for waves of length $2h$ and $3h$, as shown previously in section 3.8. Such waves do not propagate and describe oscillations of wavelengths $2h$ and $3h$. They are spurious surface-elevation modes introduced by the spatial discretization scheme. Hence, the $P_1 - P_1$ pair is usually not used to solve the SW system, unless a wave equation formulation or a stabilization procedure is employed [18, 36].

For the remaining FE pairs in Figures 4.2 and 4.3, we have r_{PH} close to 1 for small values of $|kh|$ and $|lh|$ in all directions. However, for increasing values of $|kh|$ and $|lh|$, corresponding to wavelengths ranging from $2h$ to $4h$, r_{PH} departs moderately from 1 in the OX, OY, and OD1 directions for the RT0 element (waves decelerate) and the $P_0 - P_1$ pair (waves accelerate). In the OD2 direction, except for wavelengths ranging from $2h$ to $3h$, r_{PH} strongly departs from 1 for the $P_0 - P_1$, MINI, $P_1 \text{ iso } P_2 - P_1$, and $P_2 - P_1$ pairs, and moderately for the RT0 and $P_1^{NC} - P_1$ pairs, for increasing values of $|kh|$ and $|lh|$, and the waves will accelerate.

From (3.3) and the results of section 3, we now determine the analytical and computed group velocities, $\mathbf{c}_{g,AN}$ and $\mathbf{c}_{g,CP}$, respectively, i.e., the velocity at which the energy is carried by the waves, with

$$\mathbf{c}_{g,AN} = \left(\frac{\partial \omega_{AN}}{\partial k}, \frac{\partial \omega_{AN}}{\partial l} \right), \quad \mathbf{c}_{g,CP} = \left(\frac{\partial \omega_{CP}}{\partial k}, \frac{\partial \omega_{CP}}{\partial l} \right).$$

We also calculate the directional derivatives $\mathbf{c}_{g,AN} \cdot \mathbf{d}$ and $\mathbf{c}_{g,CP} \cdot \mathbf{d}$, where $\mathbf{d}$ is a unit vector in the OX, OY, OD1, or OD2 directions. For the continuous case and the nine FE pairs of section 3, the group velocities (left panels) and the directional derivatives normalized by the factor $\sqrt{gH}$ (right panels) are shown in Figures 4.4, 4.5, and 4.6.

For the $P_1^{NC} - P_0$ and $P_2 - P_0$ pairs in Figure 4.4, the normalized directional derivatives $\mathbf{c}_{g,CP} \cdot \mathbf{d}$ unexpectedly depart from 1 in all directions for small values of $|kh|$ and $|lh|$. Hence, $\mathbf{c}_{g,CP}$ is not consistent with the analytic solution for both pairs as kh and lh tend to zero, and large inaccuracies can be expected in the speed of energy propagation. For the $P_1 - P_1$ pair in Figure 4.4, the group velocity is zero for waves of length $3h$ in the OX, OY, and OD1 directions, and for wavelengths ranging from $2h$ to $3h$ the group velocity has the wrong sign. In the OD2 direction, because the group velocity is zero three times for waves longer than $2h$, it has alternatively right and wrong signs. This is a consequence of having zero frequency for waves of length $2h$ and $3h$, as shown in section 3.8.

For the remaining pairs of Figures 4.5 and 4.6, the group velocity is consistent with the analytic solution as kh and lh are small. However, at the following values of (kh, lh), $(0, \pm\pi)$, $(\pm\pi, 0)$, $(\pm\pi, \pm\pi)$ (waves of length $2h$), we have $\mathbf{c}_{g,CP} = \mathbf{0}$ contrarily to the analytic case, and hence although waves of length $2h$ are propagating, the associated energy is not. For the RT0, $P_0 - P_1$, and MINI pairs in Figure 4.5 and for the $P_2 - P_1$ pair in Figure 4.6, we observe that $\mathbf{c}_{g,CP} \cdot \mathbf{d}$ has a negative (wrong) sign in the OD2 direction for wavelengths greater than $2h$ and smaller than $3h$. Finally, for all pairs in the OD2 direction, the magnitude of the group velocity reaches a peak ranging from 1.5 (for the $P_1^{NC} - P_1$ and RT0 pairs) to 2.5 (for the $P_0 - P_1$ pair) times the analytical value for wavelengths close to $4h$, leading to inaccuracies if such waves are generated and sustained in a numerical model.

4.2. Inertia-gravity waves and other modes. We now assume $f \neq 0$ and note $\lambda \equiv \sqrt{gH}/f$, the Rossby radius of deformation. Within a numerical factor, it is the distance covered by a wave travelling at the speed $\sqrt{gH}$ during one inertial period
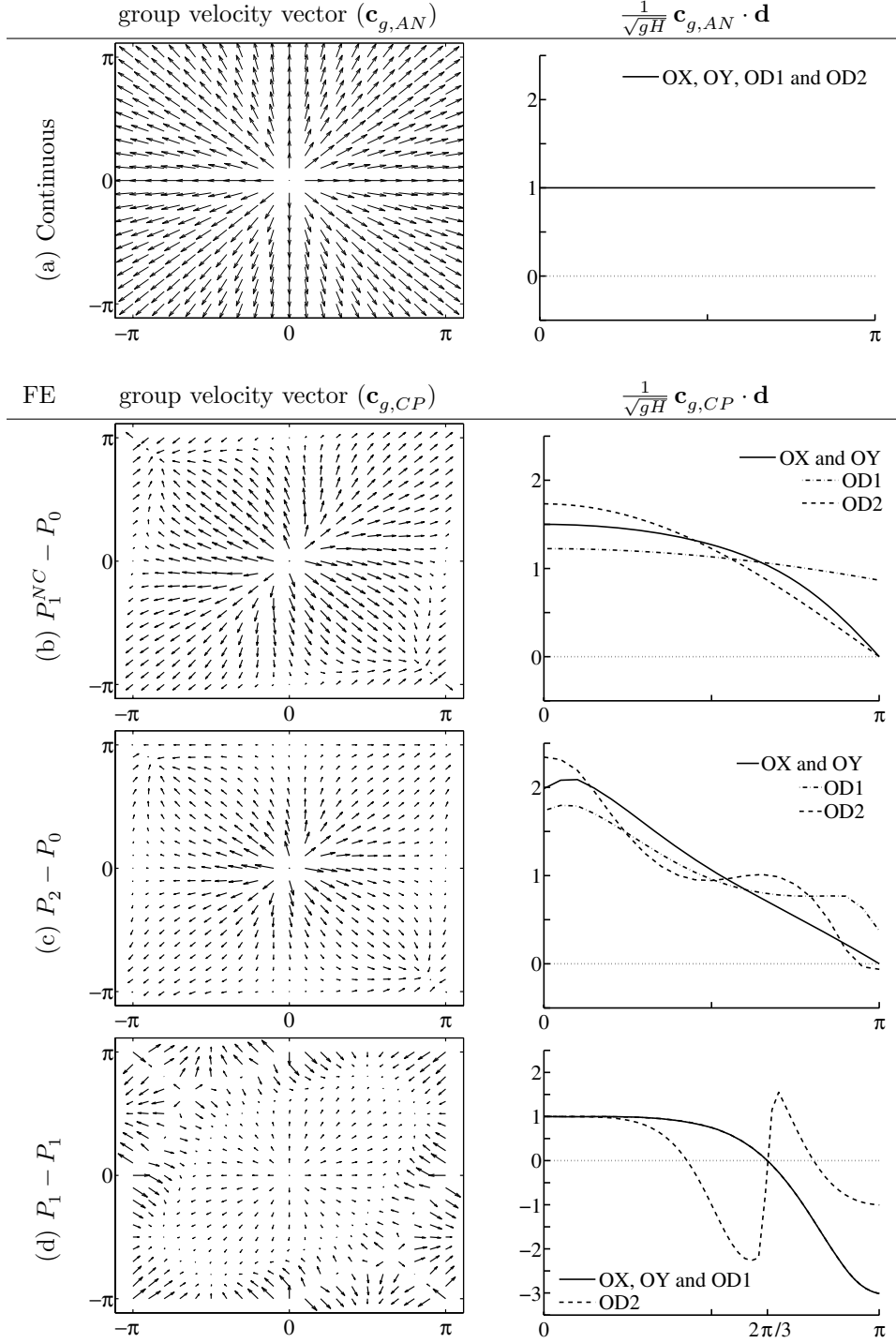
group velocity vector $(\mathbf{c}_{g,AN})$ $\frac{1}{\sqrt{gH}}\,\mathbf{c}_{g,AN}\cdot\mathbf{d}$

FE   group velocity vector $(\mathbf{c}_{g,CP})$ $\frac{1}{\sqrt{gH}}\,\mathbf{c}_{g,CP}\cdot\mathbf{d}$

FIG. 4.4. *The group velocity vector (left panels) where the Cartesian coordinate axes are* kh
and lh, *and the normalized directional derivative* $\frac{1}{\sqrt{gH}}\,\mathbf{c}_g\cdot\mathbf{d}$ *(right panels), where* $\mathbf{d}$ *is a unit vector*
in the OX, OY, OD1, or OD2 direction, for (a) *the continuous case and the* (b) $P_1^{NC}-P_0$, (c)
P_2-P_0, *and* (d) P_1-P_1 *pairs.*

FE   group velocity vector $(\mathbf{c}_{g,CP})$ $\frac{1}{\sqrt{gH}}\,\mathbf{c}_{g,CP}\cdot\mathbf{d}$
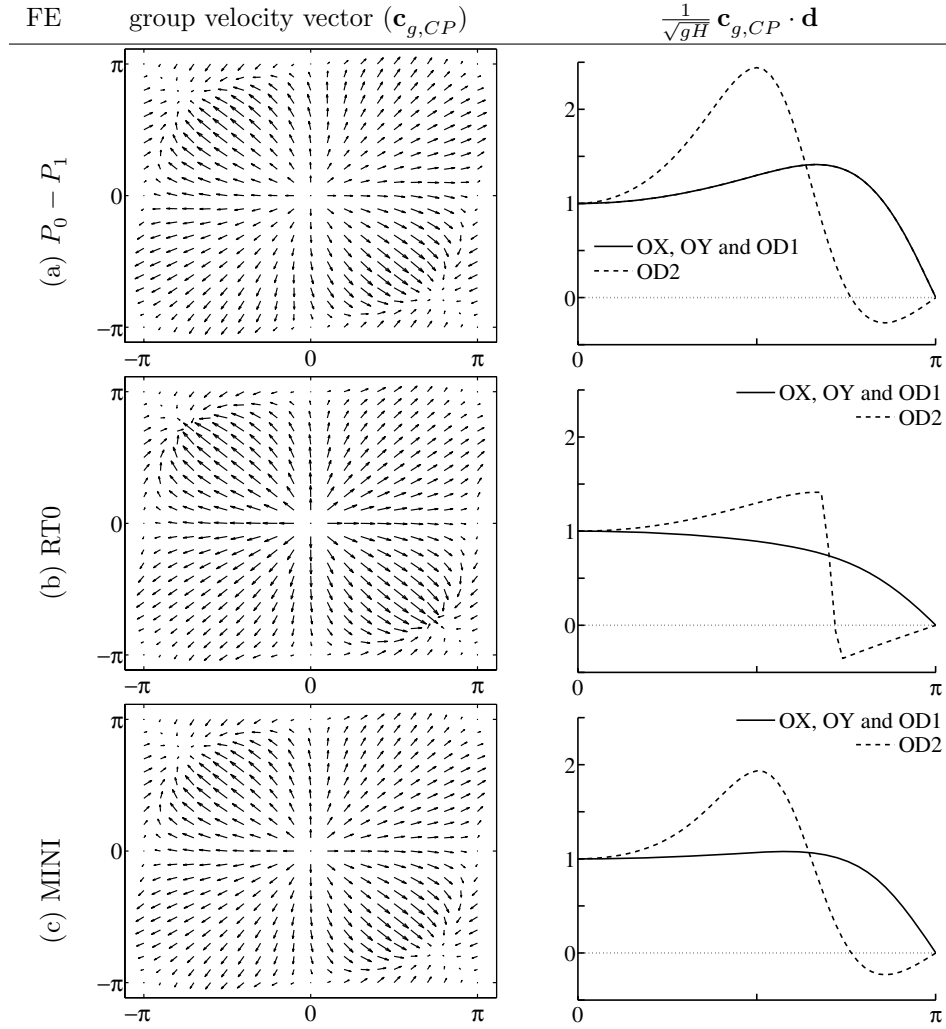
FIG. 4.5. *As for Figure* 4.4 *but for the* (a) $P_0 - P_1$, (b) *RT0, and* (c) *MINI pairs.*

$(2\pi/f)$. Using (3.3) and the results of section 3 we now obtain the phase speed ratio

$$(4.2) \qquad r_{PH}^{f} \equiv \frac{|c_{CP}|}{|c_{AN}|} = \frac{|\omega_{CP}|}{|\omega_{AN}|} = \frac{f\sqrt{1+\left(\frac{\lambda}{h}\right)^2 t(kh,lh)}}{f\sqrt{1+\left(\frac{\lambda}{h}\right)^2 (k^2h^2+l^2h^2)}},$$

where ω_{CP} corresponds to an inertia-gravity mode of type $O(1)$, as in (4.1) but now with $f \neq 0$, and $t(kh, lh)$ is a trigonometric expression depending on kh and lh.

For the $P_1 - P_1$, $P_0 - P_1$, $P_1^{NC} - P_1$, P_1 iso $P_2 - P_1$, MINI, and $P_2 - P_1$ pairs, a realistic positive value for f would have little effect on the plots of Figures 4.2 to 4.6 when $\lambda/h \gg 1$ (high resolution), as $t(kh, lh)$ is bounded in (4.2) for $0 \le kh \le \pi$ and $0 \le lh \le \pi$. Hence, we have $r_{PH}^{f} \simeq r_{PH}$ for $\lambda/h \gg 1$. In the case $\lambda/h \ll 1$ (coarse resolution), we deduce from (4.2) that $r_{PH}^{f} \simeq 1$. However, the results obtained for r_{PH} in Figures 4.2 to 4.6 are roughly preserved but at smaller scales.
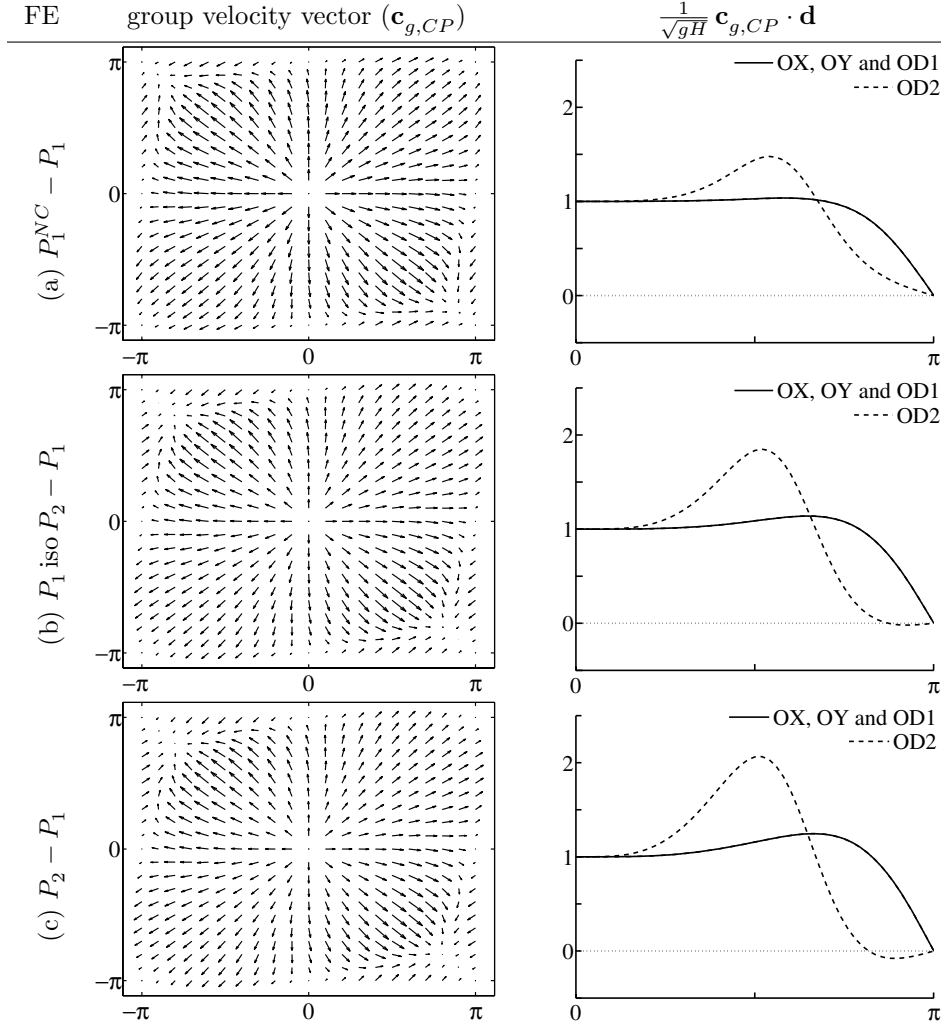
FE	group velocity vector ($\mathbf{c}_{g,CP}$)	$\frac{1}{\sqrt{gH}}\,\mathbf{c}_{g,CP}\cdot\mathbf{d}$

FIG. 4.6. *As for Figure 4.4 but for the* (a) $P_1^{NC} - P_1$, (b) $P_1 \, iso \, P_2 - P_1$, *and* (c) $P_2 - P_1$ *pairs.*

The remaining $P_1^{NC} - P_0$, $P_2 - P_0$, and RT0 pairs, as mentioned in Table 3.1, lead to discrete frequencies of type $O(\frac{1}{h})$, and additionally in $O(h)$ for the $P_2 - P_0$ pair. The nondimensional frequency ω_{CP}/f, corresponding to modes in $O(1)$, $O(\frac{1}{h})$, and $O(h)$ along selected axes (OX, OY, OD1, and OD2), is plotted for these pairs in Figures 4.7 and 4.8 and is compared with the continuous case. We consider λ/h ranging from $1/10$ (coarse resolution) to 2 (high resolution).

For the $P_1^{NC} - P_0$ and $P_2 - P_0$ pairs in Figure 4.7, the mode of type $O(\frac{1}{h})$ is a spurious mode appearing as an approximate mirror image of the mode in $O(1)$. For the $P_2 - P_0$ pair, the mode in $O(h)$ is trapped close to zero, and this is especially true when the Rossby radius is resolved (high resolution). Because the $P_2 - P_0$ pair is the only one in Table 3.1 to have a mode in $O(h)$ and no mode corresponding to the geostrophic mode $\omega = 0$ in (3.2), we suggest considering the mode in $O(h)$ as a spurious one which coincides with the geostrophic mode as mesh spacing $h \to 0$. Recall that the geostrophic mode would correspond to the slow Rossby mode on a
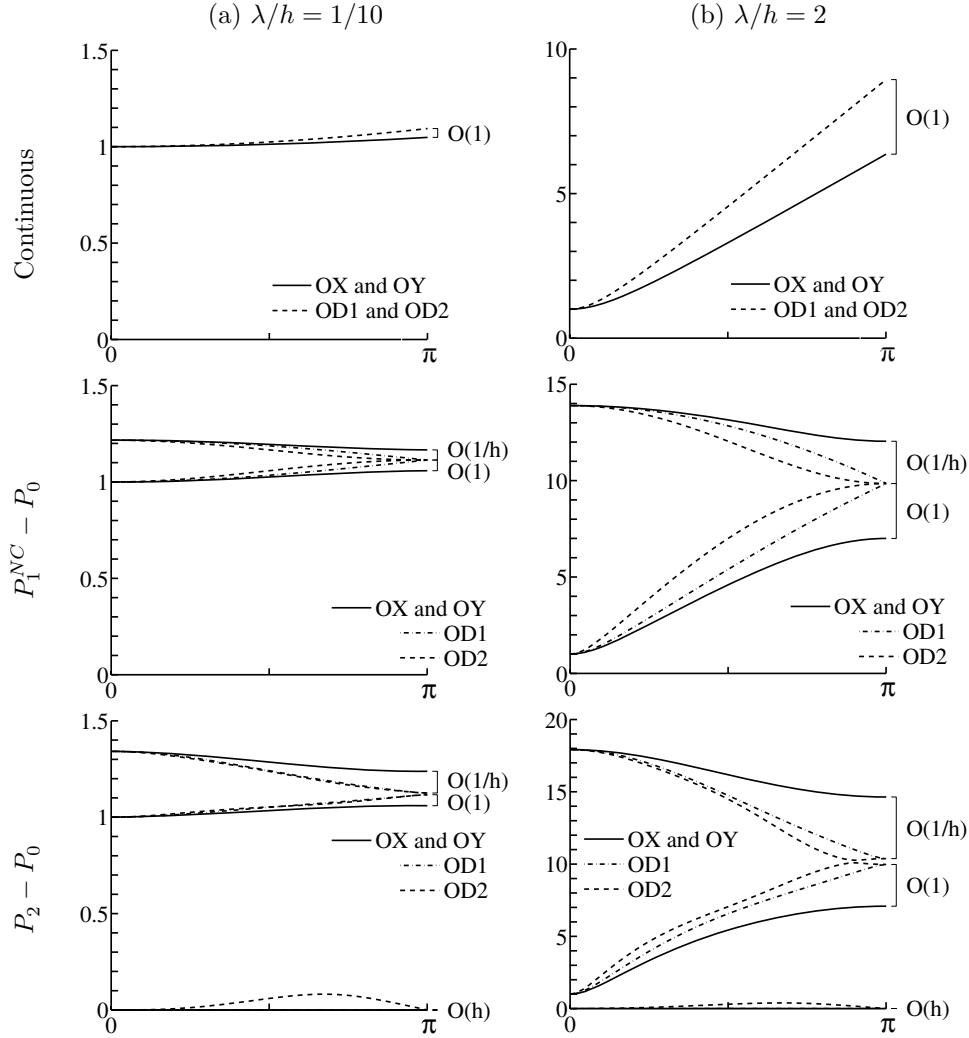
FIG. 4.7. *The nondimensional frequency ω_{CP}/f, corresponding to modes in $O(1)$, $O(\frac{1}{h})$, and $O(h)$ along selected axes (OX, OY, OD1, and OD2), for the continuous case and the $P_1^{NC} - P_0$ and $P_2 - P_0$ pairs. We note $\lambda \equiv \sqrt{gH}/f$, the radius of deformation (Rossby radius), and two cases are considered, namely, $\lambda/h = 1/10$ (coarse resolution) and $\lambda/h = 2$ (high resolution).*

β-plane.

For the RT0 pair in Figure 4.8 the mode in $O(\frac{1}{h})$ behaves quite differently from the corresponding ones for the $P_1^{NC} - P_0$ and $P_2 - P_0$ pairs in Figure 4.7. Indeed, for values of λ/h below 0.2 (obtained numerically), the mode in $O(\frac{1}{h})$ is much closer to the continuous solution in Figure 4.8 than the $O(1)$ one. Moreover, the mode in $O(1)$ is uniformly zero for all kh and lh in the inertial limit ($g = 0$, i.e., $\lambda/h = 0$), but it tends to draw closer to the continuous solution as the values of λ/h progressively increase. However, in order for the mode in $O(1)$ to be monotonic in kh and lh, as for the continuous one, λ/h has to be chosen greater than 0.45 (obtained numerically). The modes in $O(\frac{1}{h})$ and in $O(1)$ have no common intersection except locally, when $\lambda/h = 1/6$ and $kh = lh = 0$, as shown in Figure 4.8(c). Note the mode in $O(\frac{1}{h})$
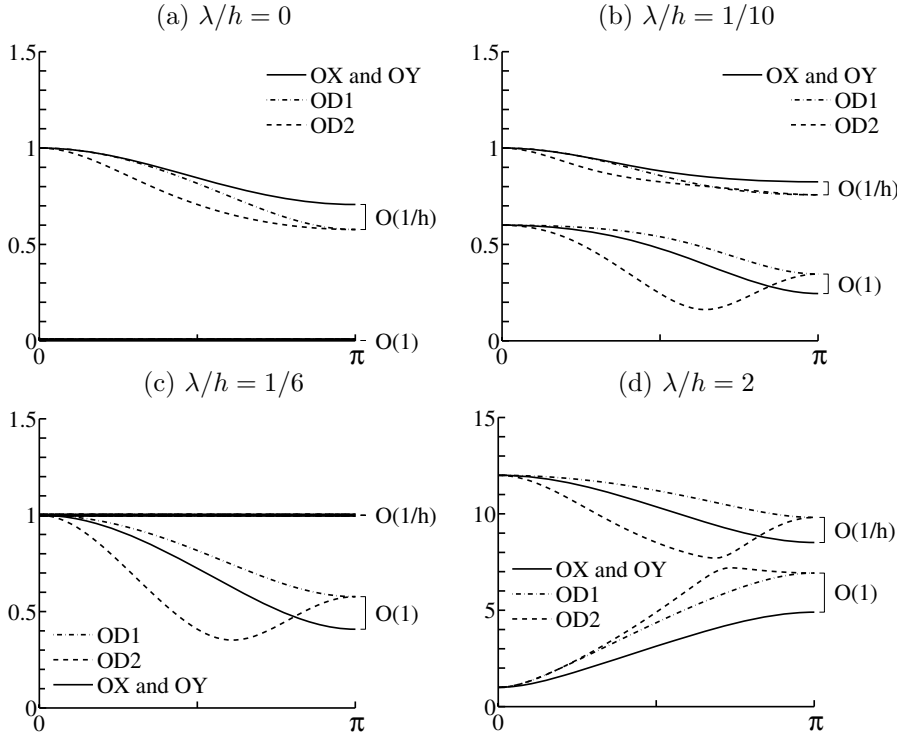
FIG. 4.8. *As for Figure* 4.7 *but for the RT*0 *element in the cases* $\lambda/h = 0$, $1/10$, $1/6$, *and* 2.

is uniformly one for all kh and lh in the case $\lambda/h = 1/6$, and as λ/h progressively increases (above $1/6$), it appears as an approximate mirror image of the mode in $O(1)$, i.e., as a spurious mode. Finally, in the OD2 direction both the $O(\frac{1}{h})$ and $O(1)$ modes exhibit nonmonotonic curves for a wide range of λ/h.

5. Numerical results. The results of two tests using (2.1) and (2.2) are now presented. The first test is performed in [11] for FD grids. It is reproduced here to examine the consequences of the distortion observed in Figure 4.8 in the dispersion relation of the RT0 element for small values of λ/h (coarse resolution).
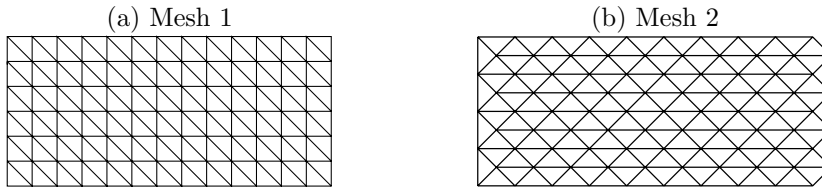

FIG. 5.1. *A window of* (a) *Mesh* 1, *made up of biased right isosceles triangles, and* (b) *Mesh* 2, *obtained from Mesh* 1 *by rotation.*

The main point of interest is to verify whether or not the RT0 discretization properly simulates the geostrophic adjustment process, in which the dispersion of the inertia-gravity waves leads to the establishment of a geostrophic balance.

The square domain extent is 5500 km × 5500 km, and it is discretized using biased right isosceles triangles (as in Figure 5.1(a)) with a uniform node spacing $h = 220$
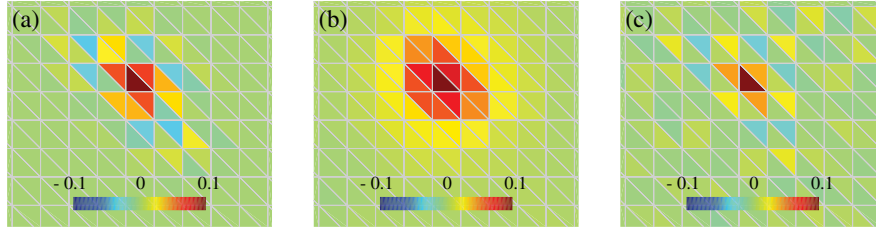
Fig. 5.2. *Window of the surface-elevation field around the point mass source (*0.1 m*) for the RT*0 *pair; after 1 day of simulation and* (a) $\lambda/h = 1/6$ *(coarse resolution),* (b) $\lambda/h = 2$ *(high resolution);* (c) *after 10 days of simulation and* $\lambda/h = 1/12$ *(coarse resolution).*
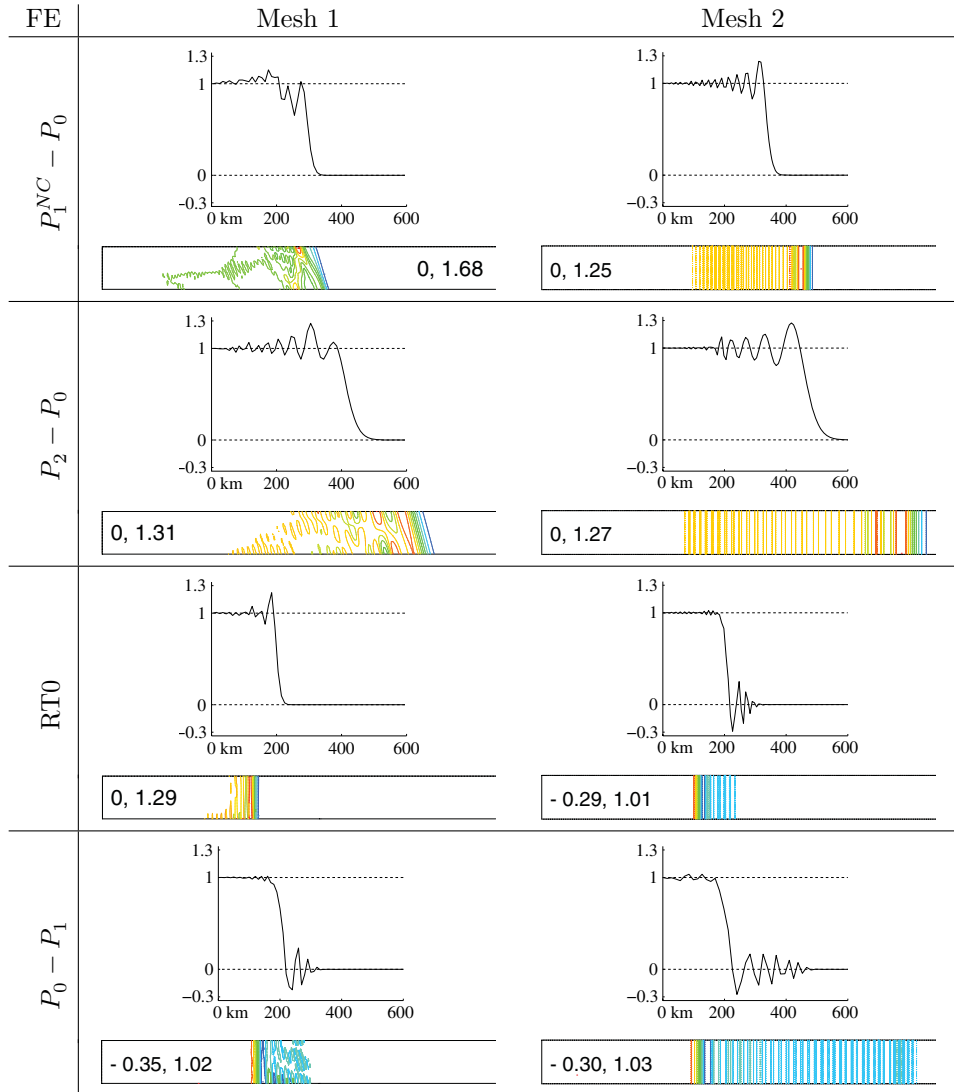

Fig. 5.3. *Vertical cross-sections (top) and isolines (bottom, over* 2550 km*) of the elevation field at times* 2000 s *and* 10000 s *of the propagation, respectively, for the* $P_1^{NC} - P_0$, $P_2 - P_0$, RT0, *and* $P_0 - P_1$ *pairs. For the isolines, the minimum and maximum values are specified in each panel.*
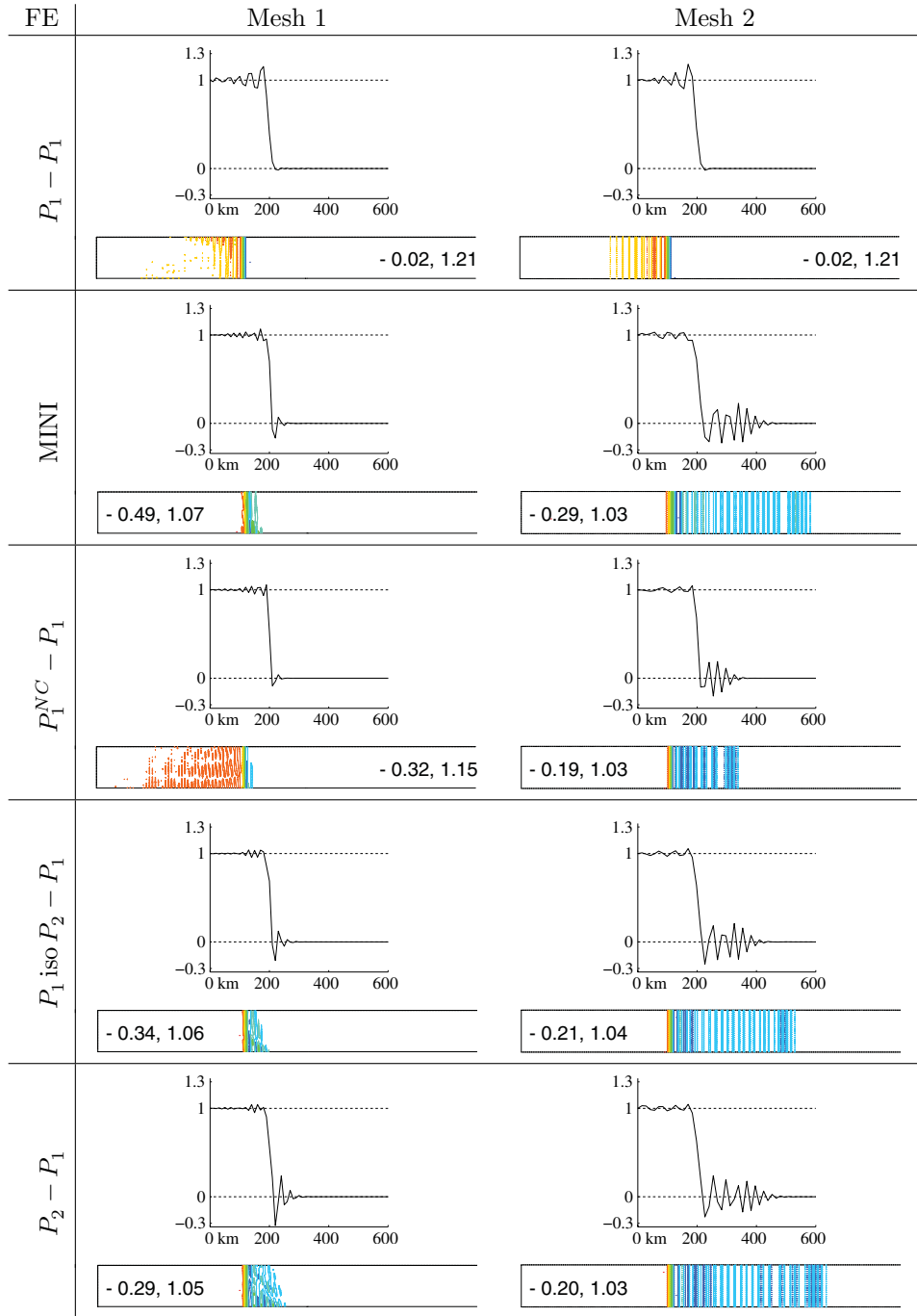
FE	Mesh 1	Mesh 2

FIG. 5.4. *As for Figure* 5.3 *for the* $P_1 - P_1$, *MINI,* $P_1^{NC} - P_1$, P_1 *iso* $P_2 - P_1$, *and* $P_2 - P_1$ *pairs.*
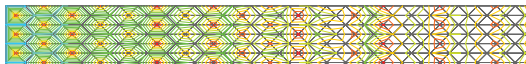

FIG. 5.5. *Isolines of the surface elevation on a window of Mesh* 2 *for the* $P_1 - P_1$ *pair at time* 10000 s *by using a linear bathymetry. As expected, a spurious mode of wavelength* 3h *is observed.*

km, leading to a 25×25 mesh. The fluid is initially at rest, and zero normal velocity is specified at the lateral boundaries. A point mass source and a point mass sink of 0.1 m and -0.1 m, respectively, are prescribed at fixed locations $12\,h$ apart at each time step; otherwise the initial surface elevation field is uniform. The Coriolis parameter is held constant and evaluated close to $45°\,\mathrm{N}$, with $f = 10^{-4}\,\mathrm{s^{-1}}$, and the time step is 450 s. The surface-elevation field is shown after one day of simulation, which is approximately the time required for geostrophic adjustment to occur, in Figures 5.2(a) and (b). In Figure 5.2(a), for $\lambda/h = 1/6$ (coarse resolution) with $\sqrt{gH} = 11/3\,\mathrm{m\,s^{-1}}$, and also for $\lambda/h \leq 1/2$, the RT0 scheme exhibits a checkerboard-like pattern of noise in the elevation field around the mass source and sink points, shown by an irregular alternation of positive and negative height areas (that are constant per triangle). Note that such a pattern is not observed for the other pairs. Due to the symmetry, only the result around the point mass source is shown. We believe the checkerboard-like appearance is probably due to the distortion observed in Figure 4.8 in the dispersion relation for small values of λ/h (coarse resolution). In Figure 5.2(b) for $\lambda/h = 2$ (high resolution) with $\sqrt{gH} = 44\,\mathrm{m\,s^{-1}}$, the surface-elevation distribution exhibits a regular and expected pattern as for the other pairs, except for the $P_1 - P_1$ one (due to the spurious surface-elevation mode). We also conducted the experiment over 10 days, and the result is shown in Figure 5.2(c) for $\lambda/h = 1/12$ (coarse resolution) with $\sqrt{gH} = 11/6\,\mathrm{m\,s^{-1}}$. The checkerboard-like pattern is more apparent than in Figure 5.2(a), particularly when considering the alternation of blue and yellow triangles surrounding the four centered ones (red and orange) in the OX, OY, and OD2 directions. Note that in all cases the gravitational Courant number is small (≤ 0.1) and the use of a forward Euler and a Crank–Nicolson time stepping schemes yields essentially the same results.

In the second test, (2.1) and (2.2) are solved using $f = 0$. The purpose of the experiment is to validate the analytical results obtained in section 4.1 on two meshes, Mesh 1 and Mesh 2, shown in Figure 5.1. Mesh 1 is made up of biased right triangles and Mesh 2 is obtained from Mesh 1 by a rotation of $\pi/4$. Such meshes are used in order to simulate gravity-wave propagation: along the OX and OY directions for Mesh 1 and along the OD2 direction for Mesh 2. The domain extent is 7000 km $\times$ 280 km for Mesh 1 and $5000\sqrt{2}$ km $\times$ $200\sqrt{2}$ km for Mesh 2. In both cases the resolution is $h = 10$ km, along the x- or y-axis for Mesh 1 and along the diagonal for Mesh 2. The fluid is initially at rest and zero normal velocity is specified at the lateral boundaries, except at the western one. The conditions $\eta = 1$ m and $u = 0.1\,\mathrm{m\,s^{-1}}$ (i.e., $u = \sqrt{\frac{g}{H}} \times 1$ m) are prescribed at each time step at the western boundary, with $H = 1000$ m and $g = 10\,\mathrm{m\,s^{-2}}$, i.e., $\sqrt{gH} = 100\,\mathrm{m\,s^{-1}}$. Note that the velocity has been imposed weakly at the western boundary for the $P_0 - P_1$ pair. The time step is set to 10 s, and the gravitational Courant number is thus 0.1.

In Figures 5.3 and 5.4 the vertical cross-sections (on the x, z-plane) and the isolines of the wave propagation are displayed for graphical convenience, after 2000 s and 10000 s, respectively, on the two meshes. For all pairs, except the $P_1^{NC} - P_0$ and $P_2 - P_0$ ones, the wave front propagates at the analytical speed $100\,\mathrm{m\,s^{-1}}$. This is because r_{PH} is close to 1 for small values of $|kh|$ and $|lh|$ in all directions as shown in Figures 4.2 and 4.3. However, the maximum values observed for r_{PH} in the OX and OD2 directions are 1.5 and 1.73, respectively, for the $P_1^{NC} - P_0$ pair, and 2.18 and 2.45, respectively, for the $P_2 - P_0$ one. For the $P_1^{NC} - P_0$ and $P_2 - P_0$ pairs, the wave front speeds are thus expected to be $150\,\mathrm{m\,s^{-1}}$ and $218\,\mathrm{m\,s^{-1}}$, respectively, in the OX direction, and $173\,\mathrm{m\,s^{-1}}$ and $245\,\mathrm{m\,s^{-1}}$, respectively, in the OD2 direction. These analytical values are in good agreement with the computed ones, observed in

Figures 5.3 and 5.4. Indeed, for the $P_1^{NC} - P_0$ and $P_2 - P_0$ pairs, the computed wave front speeds are $141 \, \mathrm{m \, s^{-1}}$ and $209 \, \mathrm{m \, s^{-1}}$, respectively, on Mesh 1, and $172 \, \mathrm{m \, s^{-1}}$ and $242 \, \mathrm{m \, s^{-1}}$, respectively, on Mesh 2, with a mesurement error of about $2 \, \mathrm{m \, s^{-1}}$. The loss of symmetry observed in the front propagation for the $P_1^{NC} - P_0$ and $P_2 - P_0$ pairs on Mesh 1 is likely due to a faster propagation in the OD2 direction. This explains the observed southeast orientation of the front and hence its partial propagation in the OD1 direction. Consequently, due to the results of Figure 4.2 in the OD1 direction, the computed wave speed is slightly smaller than the analytic one on Mesh 1. On Mesh 2, because the faster (dominant) propagation is along the OD2 direction, the front is not tilted and the analytical and computed values nearly coincide.

There is also a good agreement between the numerical dispersion observed in Figures 4.2 and 4.3 and the simulation results shown in Figures 5.3 and 5.4, except for the $P_1^{NC} - P_0$ and $P_2 - P_0$ pairs due to the incorrect position of the front. Indeed, in the OX, OY, and OD1 directions we have $r_{PH} \simeq 1$ for the $P_1^{NC} - P_1$ pair in Figure 4.3(c), and a small amount of numerical dispersion is observed in Figure 5.4 on Mesh 1. For the MINI, $P_1 \, \mathrm{iso} \, P_2 - P_1$, $P_2 - P_1$, and $P_0 - P_1$ pairs in the previous directions, r_{PH} progressively increases from 1.03 (MINI) up to 1.2 ($P_0 - P_1$) as observed in Figures 4.2 and 4.3. Hence, we have $|c_{CP}| \geq |c_{AN}|$ and increasing dispersion is noticeable upstream the front in Figures 5.3 and 5.4 for these pairs on Mesh 1. For the RT0 and $P_1 - P_1$ pairs in the previous directions, we have $r_{PH} \leq 1$ in Figures 4.2 and 4.3, and hence $|c_{CP}| \leq |c_{AN}|$, leading to dispersion effects downstream the front as shown in Figures 5.3 and 5.4 on Mesh 1. In the OD2 direction, we still have $r_{PH} \leq 1$ for the $P_1 - P_1$ pair, and oscillations are again present downstream the front on Mesh 2 as shown in Figure 5.4. For the RT0 pair we now have $r_{PH} \geq 1$ in the OD2 direction (except for small wavelengths), and the dispersion effects are noticeable upstream the front in Figure 5.3 on Mesh 2. For the $P_1^{NC} - P_1$, $P_1 \, \mathrm{iso} \, P_2 - P_1$, MINI, $P_2 - P_1$, and $P_0 - P_1$ pairs in the OD2 direction, r_{PH} progressively increases from 1.15 ($P_1^{NC} - P_1$) up to 1.7 ($P_0 - P_1$) as observed in Figures 4.2 and 4.3. We thus have $|c_{CP}| \geq |c_{AN}|$, and increasing dispersion is noticeable for these pairs upstream the front in Figures 5.3 and 5.4 on Mesh 2.

Spurious elevation modes are not observed in Figure 5.4 for the $P_1 - P_1$ pair. This is because a constant value of H is used. However, when $H = 1000$ m if $x \leq 400$ km, when $H = 800$ m if $x \geq 600$ km, and by assuming H is linear if 400 km $\leq x \leq 600$ km, a spurious surface elevation mode of wavelength $3h$ is triggered, as shown in Figure 5.5 on Mesh 2. This agrees well with the result predicted by theory in Figure 4.3(a) in the OD2 direction.

Finally, the second test has also been performed on unstructured meshes. Two main features are observed for all pairs: the numerical dispersion upstream the front is more significant than on Mesh 1 but less than on Mesh 2, and additional noise is generated downstream the front. Further, the loss of symmetry observed in the front propagation in Figure 5.3 for the $P_1^{NC} - P_0$ and $P_2 - P_0$ is only marginally present.

6. Conclusions. This appears to be the first study of the dispersion relation and spurious mode behavior for FE solutions of the two-dimensional linearized SW equations based on the examination of a variety of mixed FE pairs. For each pair the frequency wave number or dispersion relation is obtained and analyzed, and the dispersion properties are compared analytically and graphically with the continuous case to illustrate the main points of interest. Two numerical tests, concerning the propagation of gravity waves, are performed. In the first experiment, the simulation of the geostrophic adjustment process, the RT0 element exhibits a checkerboard-like pattern of noise in the elevation field when the grid resolution is low relative to the

Rossby radius of deformation. Such a pattern has not been observed for the other pairs. The second test illustrates the analytical dispersion results by simulating the propagation of pure gravity waves in a long channel. In particular, for the $P_1^{NC} - P_0$ and $P_2 - P_0$ pairs, the wave front propagates much faster than the analytical speed. These results can be compared with those in [32] for the geostrophic balance. We also notice the presence of spurious frequencies of type $O(\frac{1}{h})$ for the FE pairs having a piecewise-constant representation of the surface elevation. Such solutions have already been observed in [34], where the one-dimensional SW equations are discretized using the discontinuous Galerkin method, and they will be analyzed in a further study.

The preceding analysis illustrates how phase and group velocity accuracy can help in the selection of a spatial discretization scheme. In particular, the $P_1^{NC} - P_1$ and RT0 pairs have been identified as a promising compromise for the discretization of the inviscid linear SW equations, provided the grid resolution is high relative to the Rossby radius of deformation for the RT0 element. However, because of its restrictive nature, due to the use of constant values for h and H, such an analysis should be only one step of the selection process. The use of nonconstant h and H will be analyzed in subsequent studies. Further, the implementation of a time stepping technique can change the relative accuracy and merits of two spatial discretization schemes.

REFERENCES

[1] A. J. ADCROFT, C. N. HILL, AND J. C. MARSHALL, *A new treatment of the Coriolis terms in C-grid models at both high and low resolutions*, Mon. Wea. Rev., 127 (1999), pp. 1928–1936.

[2] V. AGOSHKOV, E. OVTCHINNIKOV, V. PENNATI, D. AMBROSI, AND F. SALERI, *Finite element, finite volume, and finite differences approximation to the shallow water equations*, in Finite Elements in Fluids, K. Morgan, E. Oñate, J. Periaux, J. Peraire, and O. C. Zienkiewicz, eds., Pineridge Press, Barcelona, Spain, 1993, pp. 1001–1009.

[3] V. AIZINGER AND C. DAWSON, *A discontinuous Galerkin method for two-dimensional flow and transport in shallow water*, Adv. in Water Res., 25 (2002), pp. 67–84.

[4] F. ALCRUDO AND P. GARCIA-NAVARRO, *A high-resolution Godunov-type scheme in finite volumes for the 2D shallow water equations*, Int. J. Numer. Methods Fluids, 16 (1993), pp. 489–505.

[5] K. ANASTASIOU AND C. T. CHAN, *Solution of the 2D shallow water equations using the finite volume method on unstructured triangular meshes*, Int. J. Numer. Methods Fluids, 24 (1997), pp. 1225–1245.

[6] A. ARAKAWA AND V. R. LAMB, *Computational design of the basic dynamical processes of the UCLA general circulation model*, Methods Comput. Phys., 17 (1977), pp. 173–265.

[7] D. N. ARNOLD, F. BREZZI, AND M. FORTIN, *A stable finite element for the Stokes equations*, Calcolo, 21 (1984), pp. 337–344.

[8] D. N. ARNOLD, F. BREZZI, B. COCKBURN, AND L. D. MARINI, *Unified analysis of discontinuous Galerkin methods for elliptic problems*, SIAM J. Numer. Anal., 39 (2002), pp. 1749–1779.

[9] J. H. ATKINSON, J. J. WESTERINK, AND J. M. HERVOUET, *Similarities between the wave equation and the quasi-bubble solutions to the shallow water equations*, Int. J. Numer. Methods Fluids, 45 (2004), pp. 689–714.

[10] J. H. ATKINSON, J. J. WESTERINK, AND R. A. LUETTICH, JR., *Two dimensional dispersion analyses of finite element approximations to the shallow water equations*, Int. J. Numer. Methods Fluids, 45 (2004), pp. 715–749.

[11] M. L. BATTEEN AND Y. J. HAN, *On the computational noise of finite-difference schemes used in ocean models*, Tellus, 33 (1981), pp. 387–396.

[12] M. BERCOVIER AND O. PIRONNEAU, *Error estimates for the finite element method solution of the Stokes problem in the primitive variables*, Numer. Math., 33 (1979), pp. 211–224.

[13] F. BREZZI AND M. FORTIN, *Mixed and Hybrid Finite Element Methods*, Springer Ser. Comput. Math. 15, Springer-Verlag, Berlin, 1991.

[14] G. F. CAREY, ED., *Finite Element Modeling of Environmental Problems*, John Wiley and Sons, Chichester, UK, 1995.

[15] S. CHIPPADA, C. N. DAWSON, M. L. MARTINEZ, AND M. F. WHEELER, *A Godunov-type finite volume method for the system of shallow water equations*, Comput. Methods Appl. Mech.

Engrg., 151 (1998), pp. 105–129.

[16] B. Choi, M. Iskandarani, J. C. Levin, and D. B. Haidvogel, *A spectral finite-volume method for the shallow-water equations*, Mon. Wea. Rev., 132 (2004), pp. 1777–1791.

[17] B. Cockburn, E. Karniadakis, and C. W. Shu, eds., *Discontinuous Galerkin Methods— Theory, Computation, and Applications*, Lect. Notes Comput. Sci. Engrg. 11, Springer-Verlag, Berlin, 2000.

[18] S. Danilov, G. Kivman, and J. Schröter, *A finite-element ocean model: Principles and evaluation*, Ocean Modelling, 6 (2004), pp. 125–150.

[19] C. Dawson and S. Chippada, *Numerical modeling of shallow water flows with wetting and drying boundaries by a finite volume method*, in Proceedings of the 1998 Annual Conference on Mission Earth: Modeling and Simulation of the Earth System, Western MultiConference, 1998, pp. 9–14.

[20] C. Dawson and J. Proft, *Coupled discontinuous and continuous Galerkin finite element methods for the depth-integrated shallow-water equations*, Comput. Methods Appl. Mech. Engrg., 193 (2004), pp. 289–318.

[21] M. G. G. Foreman, *A two-dimensional dispersion analysis of selected methods for solving the linearized shallow-water equations*, J. Comput. Phys., 56 (1984), pp. 287–323.

[22] L. P. Franca and C. Farhat, *On the limitation of bubble functions*, Comput. Methods Appl. Mech. Engrg., 117 (1994), pp. 225–230.

[23] V. Girault and P. A. Raviart, *Finite Element Methods for Navier–Stokes Equations*, Springer Ser. Comput. Math. 5, Springer-Verlag, Berlin, 1986.

[24] C. M. Gossard and R. L. Kolar, *Phase behavior of a finite volume shallow water algorithm*, in Proceedings of the CMWR XIII Volume 2: Computational Methods, Surface Water Systems, and Hydrology, L. R. Bentley et al., eds., A. A. Balkema, Rotterdam, 2000, pp. 921–928.

[25] P. Hood and C. Taylor, *Navier–Stokes equations using mixed interpolation*, in Finite Elements in Flow Problems, J. T. Oden, O. C. Zienkiewicz, R. H. Gallagher, and C. Taylor, eds., UAH Press, Huntsville, AL, 1974, pp. 121–132.

[26] M. Horritt, *Development and testing of a simple 2D finite volume model of sub-critical shallow water flow*, Int. J. Numer. Methods Fluids, 44 (2004), pp. 1231–1255.

[27] B. L. Hua and F. Thomasset, *A noise-free finite-element scheme for the two-layer shallow-water equations*, Tellus, 36 (1984), pp. 157–165.

[28] M. Iskandarani, D. Haidvogel, and J. Boyd, *A staggered spectral finite-element model for the shallow-water equations*, Int. J. Numer. Methods Fluids, 20 (1995), pp. 393–414.

[29] I. P. Kinnmark and W. G. Gray, *A two-dimensional analysis of the wave equation model for finite element tidal computations*, Internat. J. Numer. Methods Engrg., 20 (1984), pp. 369–383.

[30] P. H. LeBlond and L. A. Mysak, *Waves in the Ocean*, Elsevier, Amsterdam, 1978.

[31] C. Le Provost and P. Vincent, *Finite Element for Modeling Ocean Tides*, in Tidal Hydrodynamics, B. Parker, ed., John Wiley and Sons, New York, 1991, pp. 41–60.

[32] D. Y. Le Roux, A. Staniforth, and C. A. Lin, *Finite elements for shallow-water equation ocean models*, Mon. Wea. Rev., 126 (1998), pp. 1931–1951.

[33] D. Y. Le Roux, C. A. Lin, and A. Staniforth, *A semi-implicit semi-Lagrangian finite-element shallow-water ocean model*, Mon. Wea. Rev., 128 (2000), pp. 1384–1401.

[34] D. Y. Le Roux and G. F. Carey, *Stability/dispersion analysis of the discontinuous Galerkin linearized shallow-water system*, Int. J. Numer. Methods Fluids, 48 (2005), pp. 325–347.

[35] D. Y. Le Roux, *Dispersion relation analysis of the $P_1^{NC} - P_1$ finite-element pair in shallow-water models*, SIAM J. Sci. Comput., 27 (2005), pp. 394–414.

[36] D. R. Lynch and W. G. Gray, *A wave-equation model for finite-element tidal computations*, Comput. Fluids, 7 (1979), pp. 207–228.

[37] R. Mullen and T. Belytschko, *Dispersion analysis of finite element semidiscretizations of the 2-dimensional wave equation*, Internat. J. Numer. Methods Engrg., 18 (1982), pp. 11–29.

[38] G. W. Platzman, *Some response characteristics of finite element tidal models*, J. Comput. Phys., 40 (1981), pp. 36–63.

[39] D. A. Randall, *Geostrophic adjustment and the finite-difference shallow-water equations*, Mon. Wea. Rev., 122 (1994), pp. 1371–1377.

[40] P. Raviart and J. Thomas, *A mixed finite element method for 2nd order elliptic problems*, in Mathematical Aspects of the Finite Element Methods, Lecture Notes in Math. 606, I. Galligani and E. Magenes, eds., Springer-Verlag, Berlin, 1977, pp. 292–315.

[41] D. Schwanenberg and J. Köngeter, *A discontinuous Galerkin method for the shallow-water equations with source terms*, in Discontinuous Galerkin Methods—Theory, Computation,

and Applications, B. Cockburn, E. Karniadakis, and C. W. Shu, eds., Lect. Notes Comput. Sci. Engrg. 11, Springer-Verlag, Berlin, 2000, pp. 419–424.

[42] C. M. Szpilka and R. L. Kolar, *Numerical analogs to Fourier and dispersion analysis: Development, verification, and application to the shallow water equations*, Adv. in Water Res., 26 (2003), pp. 649–662.

[43] M. Taylor, J. Tribbia, and M. Iskandarani, *The spectral element method for the shallow water-equations on the sphere*, J. Comput. Phys., 130 (1997), pp. 92–108.

[44] R. A. Walters and R. T. Cheng, *Accuracy of an estuarine hydrodynamic model using smooth elements*, Water Resources Res., 16 (1980), pp. 187–195.

[45] R. A. Walters and G. F. Carey, *Analysis of spurious oscillation modes for the shallow-water and Navier–Stokes equations*, Comput. Fluids, 11 (1983), pp. 51–68.

[46] R. A. Walters, *A three-dimensional finite-element model for coastal and estuarine circulation*, Continent. Shelf Res., 12 (1992), pp. 83–102.

[47] R. A. Walters and V. Casulli, *A robust, finite-element model for hydrostatic surface water flows*, Commun. Numer. Meth. Engrg., 14 (1998), pp. 931–940.

[48] R. T. Williams and O. C. Zienkiewicz, *Improved finite-element forms for the shallow-water wave equations*, Int. J. Numer. Methods Fluids, 1 (1981), pp. 81–97.